



저작자표시-비영리-변경금지 2.0 대한민국

이용자는 아래의 조건을 따르는 경우에 한하여 자유롭게

- 이 저작물을 복제, 배포, 전송, 전시, 공연 및 방송할 수 있습니다.

다음과 같은 조건을 따라야 합니다:



저작자표시. 귀하는 원저작자를 표시하여야 합니다.



비영리. 귀하는 이 저작물을 영리 목적으로 이용할 수 없습니다.



변경금지. 귀하는 이 저작물을 개작, 변형 또는 가공할 수 없습니다.

- 귀하는, 이 저작물의 재이용이나 배포의 경우, 이 저작물에 적용된 이용허락조건을 명확하게 나타내어야 합니다.
- 저작권자로부터 별도의 허가를 받으면 이러한 조건들은 적용되지 않습니다.

저작권법에 따른 이용자의 권리는 위의 내용에 의하여 영향을 받지 않습니다.

이것은 [이용허락규약\(Legal Code\)](#)을 이해하기 쉽게 요약한 것입니다.

[Disclaimer](#)

**Master of Science**

**Uncertainty Quantification of GEKO Model Coefficients on  
Compressible Flows**

**The Graduate School of University of Ulsan**

**Department of Mechanical**

**Engineering Yeong-Ki Jung**

**Uncertainty Quantification of GEKO Model Coefficients on  
Compressible Flows**

**Academic advisor : Professor Kyoungsik Chang**

**A Thesis presented to  
the Graduate School of University of Ulsan  
In partial Fulfillment of the Requirements  
for the Degree of  
Master of Science**

**by**

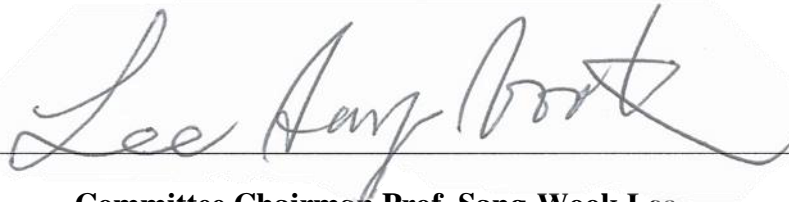
**Yeong-Ki Jung**

**Department of Mechanical Engineering  
University of Ulsan, Republic of Korea**

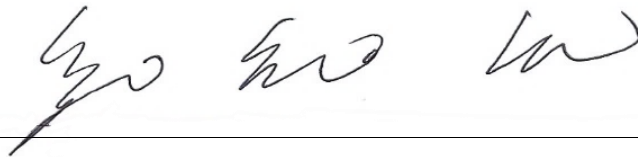
**December 2020**

# Uncertainty Quantification of GEKO Model Coefficients on Compressible Flows

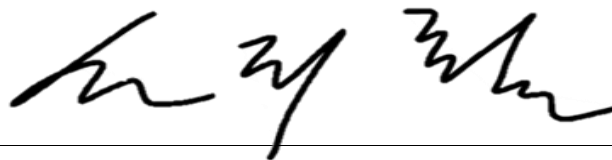
This certifies that the master thesis of Yeong-Ki Jung is approved.



Committee Chairman Prof. Sang-Wook Lee



Committee Member Prof. Kyongsik Chang



Committee Member Prof. Ji-Cheol Shin

Department of Mechanical Engineering

University of Ulsan, Republic of Korea

December 2020

**Dedicated to my parents, Ki Hwan Jung and Hyeon Suk Son**

# Contents

CONTENTS .....	I
LIST OF FIGURES .....	II
LIST OF TABLES .....	III
CHAPTER 1. INTRODUCTION .....	1
1.1 INTRODUCTION .....	1
CHAPTER 2. NUMERICAL METHODS .....	3
2.1 TURBULENCE MODELS .....	3
2.1.1 Generalized $k-\omega$ (GEKO) model .....	3
2.1.2 Baseline (BSL) $k-\omega$ model .....	6
2.1.3 Shear-Stress Transport (SST) $k-\omega$ model .....	7
2.1.4 Realizable $k-\varepsilon$ model .....	8
2.2 DISCRETIZATION SCHEMES .....	10
2.2.1 Third-Order MUSCL Scheme .....	10
2.2.2 Implicit Discretization Scheme .....	11
2.2.3 Flux type .....	12
CHAPTER 3. THEORETICAL BACKGROUND FOR UNCERTAINTY QUANTIFICATION .....	13
3.1 THE DEFINITION OF UNCERTAINTY QUANTIFICATION .....	13
3.2 POLYNOMIAL CHAOS EXPANSIONS .....	13
3.3 SAMPLING METHOD .....	16
3.4 SURROGATE MODEL .....	17
3.5 BAYESIAN INFERENCE .....	17
3.6 LIKELIHOOD .....	18
3.7 MARKOV CHAIN MONTE CARLO (MCMC) .....	19
CHAPTER 4. DETERMINISTIC SIMULATIONS .....	20
4.1 GEOMETRY .....	20
4.2 MESH .....	20
4.3 BOUNDARY CONDITIONS .....	22
4.4 RESULTS .....	23
4.4.1 Grid test .....	23
4.4.2 Base Flow .....	27
4.4.3 24-deg Compression Ramp .....	30
CHAPTER 5. UNCERTAINTY QUANTIFICATION FOR COMPRESSIBLE FLOWS .....	34
5.1 gPCE RESULTS .....	34
5.2 BAYESIAN INFERENCE .....	36
CHAPTER 6. CONCLUSION .....	41
6.1 CONCLUSIONS .....	41
6.2 FUTURE WORKS .....	42
REFERENCES .....	43

## List of Figures

<b>Fig. 1</b> Axisymmetric base flow computational grid, Closeup view of grid (bottom).....	21
<b>Fig. 2</b> 24-deg compression ramp computational grid (left), Closeup view of grid (right).....	21
<b>Fig. 3</b> Boundary Conditions (Base flow : up, Ramp flow : bottom) .....	22
<b>Fig. 4.</b> Grid sensitivity test for base flow / Pressure distribution (left), Centerline velocity (right).....	24
<b>Fig. 5.</b> Grid sensitivity test for compression ramp flow / Nondimensional pressure distribution (left), Skin friction coefficient distribution (right).....	25
<b>Fig. 6.</b> Extrapolation values from GCI w.r.t QOIs. Base flow(a, b), Compression ramp flow(c, d) / Red (Mod_ASME), Blue (SLS-GCI), filled triangle (1, 2, 3), circle (2, 3, 4), square (3,4,5), empty triangle (1, 3, 5).....	26
<b>Fig. 7.</b> Velocity profiles at 1 mm upstream from base edge.....	27
<b>Fig. 8.</b> Pressure distributions along base radius.....	28
<b>Fig. 9.</b> Static pressure contour (GEKO-CC : up, GEKO : down).....	28
<b>Fig. 10.</b> Centerline velocity.....	29
<b>Fig. 11.</b> Mach contour (left), Turbulent viscosity ratio (right).....	29
<b>Fig. 12.</b> Nondimensional pressure distribution along the bottom surface.....	31
<b>Fig. 13.</b> Skin friction coefficient distribution along the bottom surface.....	31
<b>Fig. 14.</b> Mach number contour over 24-deg compression ramp.....	32
<b>Fig. 15.</b> Static pressure contour over 24-deg compression ramp.....	33
<b>Fig. 16.</b> $C_{P_{base}}$ and RP histogram according to order of polynomial chaos.....	35
<b>Fig. 17.</b> Posterior distribution for $C_{P_{base}}$ and RP from OLS.....	37
<b>Fig. 18.</b> Posterior distribution for $C_{P_{base}}$ and RP from LARS.....	37
<b>Fig. 19.</b> Posterior distribution for SP and RP from OLS.....	37
<b>Fig. 20.</b> Posterior distribution for SP and RP from LARS.....	38
<b>Fig. 21.</b> Pressure distribution (left) and Centerline velocity (right).....	39
<b>Fig. 22.</b> Nondimensional pressure (left) and skin friction coefficient (right) distribution.....	39

## List of Tables

<b>Table 1.</b> Model coefficients of GEKO model.....	5
<b>Table 2.</b> The advantages and disadvantages of the explicit scheme and implicit scheme.....	11
<b>Table 3.</b> Classical families of orthogonal polynomials.....	14
<b>Table 4.</b> Grid independence test (Axisymmetric base flow) .....	24
<b>Table 5.</b> Grid independence test (Compression ramp) .....	24
<b>Table 6.</b> GCI $U_g$ values.....	25
<b>Table 7.</b> GCI $U_e$ values.....	25
<b>Table 8.</b> Extrapolation values from GCI.....	26
<b>Table 9.</b> Boundary layer thickness.....	30
<b>Table 10.</b> the number of sample (left), $\epsilon_{LOO}$ (right), $P$ : order of polynomial chaos, $n_p$ : oversampling rate.....	34
<b>Table 11.</b> $P$ , $\epsilon_{LOO}$ and Sobol indices of GEKO closure coefficients for QOIs.....	36
<b>Table 12.</b> Correlated model coefficients corresponding QOIs.....	36
<b>Table 13.</b> Value and error of QOIs corresponding to each calibrated model (Base flow).....	39
<b>Table 14.</b> Value and error of QOIs corresponding to each calibrated model (Ramp flow).....	40



## Abstract

# Uncertainty Quantification of GEKO Model Coefficients on Compressible Flows

In the present work, supersonic flows over an axisymmetric base and 24-deg compression ramp are investigated using Generalized  $k$ - $\omega$  (GEKO) model included in commercial package of ANSYS FLUENT. GEKO is a two-equation model, based on the  $k$  -  $\omega$  formulation, and able to be tuned for a variety of flows. Compressibility correction is applied to a turbulence model to improve a pressure level along the base surface.

Uncertainty Quantification analysis (UQ) is incorporated to quantify the uncertainty of the model coefficients and to calibrate the coefficients for the base and 24-deg compression ramp flow. Latin Hypercube Sampling (LHS) method is used for sampling input parameters which are independent as a uniform distribution. Metamodel is constructed by using ordinary least-squares (OLS) and least angle regression (LARS) and both algorithms are compared to assess fidelity of models. Affine Invariant Ensemble Algorithm (AIES) is selected to characterize the posterior via Markov Chain Monte Carlo sampling.

Through Forward problem, the most influential coefficient among the coefficients of GEKO model is known. Calibrated model coefficients are obtained through Backward problem. The results obtained using the calibrated coefficients by UQ corresponding to each flow show better agreement against available experimental measurements than obtained using default coefficients.

**Keywords:** Axisymmetric Base Flow, 24-deg Compression Ramp, Generalized  $k$ - $\omega$  model (GEKO), Polynomial Chaos Expansion (PCE), ordinary least-squares (OLS), Least Angle Regression (LARS), Uncertainty Quantification (UQ)

# Chapter 1. Introduction

## 1.1 Introduction

Controlling supersonic flows is challenging but crucial for many kinds of engineering problems, such as rockets, airplanes, missiles, projectiles. Hence, many researchers have experimentally or numerically studied flows including subsonic, transonic, supersonic, and even hypersonic speeds. An interesting and important phenomena of the high Reynolds number flows is shock-wave / boundary layer interaction (SWBLI). It occurs in a transonic, supersonic and hypersonic flight condition. Predicting SWBLI phenomena accurately is an important factor in the design of high-speed flight vehicles. On the exterior flow over the aircraft, SWBLI is able to cause loss of control, some peaks on surface thermal loading. In internal flows, it can enhance distortion and pressure losses, and even catastrophic events which are leading engine unstart. There are many supersonic cases such as a base flow, ramp, double cone, impinging shock, etc. Base flow and compression ramp flow are investigated in this present work.

For the supersonic base flow, the main issue is drag. A supersonic body experiences major drag from skin friction drag, wave drag, and pressure drag. If the drag is able to be controlled, stability and control of vehicles can be more enhanced. Hence, the predicting base drag accurately is the crucial one of the various tasks about the supersonic flows over a cylindrical afterbody. As for an experiment of the supersonic base flow, Herrin and Dutton [1] experimented on a supersonic axisymmetric base flow at  $M_\infty=2.46$ . Many researchers have tried to analyze the supersonic base flow by using computational fluid dynamics (CFD). Forsythe et al. [2] used Reynolds-averaged Navier-Stokes (RANS) and Detached-Eddy Simulation (DES) with a compressibility correction to analyze the supersonic base flow. The simulation by Simon et al. [3], Large-Eddy Simulation, Zonal Detached-Eddy Simulation (ZDES), DES and RANS have been used with different values of  $C_{DES}$ . Kawai and Fujii [4] also used LES and RANS and showed a good agreement with experimental data. But DES and LES require massive runs to achieve reasonable results compared to RANS. That is a reason why RANS are widely used for an engineering area.

Tucker and Shyy [5], Papp and Ghia [6] used  $k-\epsilon$  models to simulate the compressible base flows. Just mentioned before, Forsythe et al. [2] and kawai and Fujii [4] also used

Spalart-Allmaras (SA) model which is one of the RANS for the supersonic base flow. All of RANS models have failed to predict decent base pressure levels compared to experiment data. However, many researches have applied with compressibility correction have been investigated to improve the performances. Also various compressibility corrections have been studied and proposed. Tucker and Shyy [5] applied the compressibility correction to  $k-\varepsilon$  model and showed a higher base pressure. Simon et al. [7] used Spalart-Allmaras model applied with several compressibility corrections and obtained the averaged pressure coefficient which is closer to the experimental data than using the models not including the compressibility corrections. But they also mentioned that such corrections led to an overestimation of the reattachment length and an underestimation of the shear layer development. Some compressibility corrections are able to improve the physics prediction of such flows by lowering the turbulent eddy viscosity production. These fixes produce results in averaged base pressure levels that more closely match the experimental data [2, 5, 6, 7] but variations along the base radius are enhanced.

However, all of the applications applied with compressibility correction could not always show satisfactory results for all types of compressible flows. For the compression ramp simulation, Wilcox [8] obtained the good agreement without introducing any compressibility modifications to the turbulence model for Mach 2 flow past a backward-facing step, Mach 3 compression corners and reflecting shocks, etc. Wilcox [8] also mentioned that, applying a dilatation-dissipation modification to the  $k$  equation improves compressible mixing-layer predictions [9] but it is omitted from the  $k$  equation for general applications because it has a detrimental effect on shock-separated-flow predictions. Another paper written by Wilcox [10] mentioned that the compressibility corrections cause a decrease in the effective von Kármán constant, which yields that unwanted decrease in skin friction. Rizzetta [11] also mentioned that the compressibility corrections such as the  $k - \varepsilon$  equations which account for dilatation-dissipation and/or pressure-dilatation fluctuation can degrade performance in near-wall regions of attached flows [13]. Gerolymos et al. [14] did not include direct compressibility effects and pressure-dilatation for compression ramp simulation. Hence, in this thesis, the compressibility correction is applied to turbulence models only for the axisymmetric base flow case.

## Chapter 2. Numerical Methods

In this chapter, the numerical method used in present work is explained. The current work incorporates Generalized  $k$ - $\omega$  (GEKO), Baseline (BSL)  $k$ - $\omega$ , Shear-Stress Transport (SST)  $k$ - $\omega$ , Realizable  $k$ - $\varepsilon$  model in FLUENT [15].

### 2.1 Turbulence models

#### 2.1.1 Generalized $k$ - $\omega$ (GEKO) model

The characteristic of the GEKO model is that the model coefficients of the model are able to be controlled for tuning the model to various flow scenarios. In this present work, three model coefficients are considered for compressible flows.

GEKO model formulation is following as :

$$\frac{\partial(\rho k)}{\partial t} + \frac{\partial(\rho U_j k)}{\partial x_j} = P_k - C_\mu \rho k \omega + \frac{\partial}{\partial x_j} \left[ \left( \mu + \frac{\mu_t}{\sigma_k} \right) \frac{\partial k}{\partial x_j} \right] \quad (2.1)$$

$$\frac{\partial(\rho \omega)}{\partial t} + \frac{\partial(\rho U_j \omega)}{\partial x_j} = C_{\omega 1} F_1 \frac{\omega}{k} P_k - C_{\omega 2} F_2 \rho \omega^2 + \rho F_3 CD + \frac{\partial}{\partial x_j} \left[ \left( \mu + \frac{\mu_t}{\sigma_\omega} \right) \frac{\partial \omega}{\partial x_j} \right] \quad (2.2)$$

$$\mu_t = \rho \nu_t = \rho \frac{k}{\max(\omega, S/C_{Realize})} \quad (2.3)$$

$$P_k = -\tau_{ij} \frac{\partial U_i}{\partial x_j} \quad (2.4)$$

$$\tau_{ij}^{EV} = -\rho \overline{u'_i u'_j} = \mu_t 2S_{ij} - \frac{2}{3} \rho k \delta_{ij} \quad (2.5)$$

$$CD = \frac{2}{\sigma_\omega} \frac{1}{\omega} \frac{\partial k}{\partial x_j} \frac{\partial \omega}{\partial x_j} \quad (2.6)$$

$$\tau_{i,j} = \tau_{ij}^{EV} - C_{CORNER} \frac{1.2\mu_t}{\max(0.3\omega\sqrt{0.5(S^2 + \Omega^2)})} (S_{ik}\Omega_{kj} - \Omega_{ik}S_{kj}) \quad (2.7)$$

where

$$S_{ij} = \frac{1}{2} \left( \frac{\partial U_i}{\partial x_j} + \frac{\partial U_j}{\partial x_i} \right), \Omega_{ij} = \frac{1}{2} \left( \frac{\partial U_i}{\partial x_j} - \frac{\partial U_j}{\partial x_i} \right), S = \sqrt{2S_{ij}S_{ij}}, \Omega = \sqrt{2\Omega_{ij}\Omega_{ij}} \quad (2.8)$$

The coefficients of the GEKO model are implemented through the functions ( $F_1, F_2, F_3$ ) which can be controlled to achieve different goals in a variety of parts of the computational domain. There are six parameters included, which are :

- $C_{SEP}$ 
  - Main parameter for adjusting separation prediction for boundary layers.
  - Affects all flows : Increasing  $C_{SEP}$  reduces eddy-viscosity leading to more sensitivity to adverse pressure gradients for boundary layers and to lower spreading rates for free shear flows.
- $C_{NW}$ 
  - Affects mostly the inner part of wall boundary layers (no impact on free shear flows)
  - Increasing  $C_{NW}$  leads to higher wall shear stress and wall heat transfer rates in non-equilibrium flows.
- $C_{MIX}$ 
  - Affects only free shear flows ( boundary layer shielded due to function  $F_{blend}$  which is discussed later).
  - Increasing  $C_{MIX}$  increases spreading rates of free shear flows.
  - For each value of  $C_{SEP}$  an optimal value of  $C_{MIX}$  exists, which maintains optimal free shear flow. This value is given by the correlation  $C_{MIX}=C_{MixCor}$  which is default.

$$C_{MixCor} = 0.35 \text{sign}(C_{SEP} - 1) \sqrt{(|C_{SEP} - 1|)} \quad (2.9)$$

- $C_{JET}$ 
  - Is active in a sub-model of  $C_{MIX}$  (no impact when  $C_{MIX}$  is equal to 0)
  - Affects mostly jet flows. Increasing  $C_{JET}$  while  $C_{MIX}$  is active, decreases spreading rate for jets.
  - Allows to adjust spreading rate of jet flows while maintaining spreading rate of mixing layer
- $C_{CORNER}$ 
  - Non-linear stress-strain term to account for secondary flows in corners (e.g. wing-body junctions etc.)
- $C_{CURV}$ 
  - An existing model for curvature correction, which can be combined with the GEKO model

All coefficients can be accessed globally or locally by using User Defined Functions (UDFs) which is allowing a global or zonal model optimization.

The coefficients  $C_{MIX}$  and  $C_{JET}$  are designed for free shear flows, whereas  $C_{SEP}$  and  $C_{NW}$  affect boundary layers. In order to avoid any influence of  $C_{MIX}$  and  $C_{JET}$  onto

boundary layers, a blending function is incorporated, which deactivates  $C_{MIX}$  and  $C_{JET}$  in the boundary layer. The blending function is given by :

$$L_T = \frac{\sqrt{\tilde{k}}}{C_\mu \omega} \quad (2.10)$$

$$\tilde{k} = \max(k, CFb_{Lam} \cdot \omega) \quad (2.11)$$

$$x_{blend} = CFb_{Turb} \frac{L_T}{y} \quad (2.12)$$

$$F_{GEKO} = \tanh(x_{blend}^4) \quad (2.13)$$

This function activates following the shear flow parameters :

$$F_{Free} = C_{MIX} F_{Jet}(C_{JET})(1 - F_{Blend}) \quad (2.14)$$

There are two important aspects to  $F_{Blend}$ . Firstly, the function  $F_{Blend} = 1$  inside boundary layers which means the function  $F_{Free}$  becomes equal '0'. Secondly, the parameter  $C_{JET}$  is a sub-parameter of  $C_{MIX}$ . As mentioned above, it only affects the simulation in case  $C_{MIX} \neq 0$ . The model coefficients should be in the range (Table 1). The min and max values of  $C_{MIX}$  are only suggestions by [16]. There might be situations where values lower than min (0.5) or higher than max (1.0) can be appropriate for specific flows. In order to avoid negative effects on free mixing layers by changes in  $C_{SEP}$ , however, a use of  $C_{MixCor}$  (Eq. 2.9) is recommended.

**Table 1.** Model coefficients of GEKO model

MIN		Parameter	MAX		Default
0.7	≤	$C_{SEP}$	≤	2.5	1.75
-2.0	≤	$C_{NW}$	≤	2.0	0.50
... 0.5	≤	$C_{MIX}$	≤	1.0...	$C_{MixCor}$
0.0	≤	$C_{JET}$	≤	1.0	0.90
0.0	≤	$C_{CORNER}$	≤	1.5	1.00
0.0	≤	$C_{CURV}$	≤	1.5	1.00

### 2.1.2 Baseline (BSL) $k$ - $\omega$ model

The baseline (BSL)  $k$ - $\omega$  model is a two-equation, was developed by Menter [17] to effectively blend the accurate formulation of the  $k$ - $\omega$  model in the near-wall region with the freestream independence of the  $k$ - $\varepsilon$  model in the far field. To achieve this, the  $k$ - $\varepsilon$  model is converted into a  $k$ - $\omega$  formulation by a blending function. The transport equations for the BSL  $k$ - $\omega$  model are :

$$\frac{D}{Dt}(\rho k) = \frac{\partial}{\partial x_j} \left[ \left( \mu + \frac{\mu_t}{\sigma_k} \right) \frac{\partial k}{\partial x_j} \right] - \rho \overline{u'_i u'_j} \frac{\partial u_j}{\partial x_i} - \rho \beta^* k \omega \quad (2.15)$$

$$\frac{D}{Dt}(\rho \omega) = \frac{\partial}{\partial x_j} \left[ \left( \mu + \frac{\mu_t}{\sigma_\omega} \right) \frac{\partial \omega}{\partial x_j} \right] - \frac{\alpha \alpha^*}{\nu_t} \rho \overline{u'_i u'_j} \frac{\partial u_j}{\partial x_i} - \rho \beta \omega^2 + 2(1 - F_1) \rho \frac{1}{\omega \sigma_{\omega,2}} \frac{\partial k}{\partial x_j} \frac{\partial \omega}{\partial x_j} \quad (2.16)$$

where

$$\alpha = \frac{\alpha_\infty}{\alpha^*} \left( \frac{\alpha_0 + \frac{Re_t}{R_\omega}}{1 + \frac{Re_t}{R_\omega}} \right), \sigma_k = \frac{1}{\frac{F_1}{\sigma_{k,1}} + \frac{(1 - F_1)}{\sigma_{k,2}}}, \sigma_\omega = \frac{1}{\frac{F_1}{\sigma_{\omega,1}} + \frac{(1 - F_1)}{\sigma_{\omega,2}}} \quad (2.17)$$

$$\alpha_\infty = F_1 \alpha_{\infty,1} + (1 - F_1) \alpha_{\infty,2}, \alpha_{\infty,1} = \frac{\beta_{i,1}}{\beta_\infty^*} - \frac{\kappa^2}{\sigma_{\omega,1} \sqrt{\beta_\infty^*}}, \alpha_{\infty,2} = \frac{\beta_{i,2}}{\beta_\infty^*} - \frac{\kappa^2}{\sigma_{\omega,2} \sqrt{\beta_\infty^*}}$$

From Eq. (2.15)

$$\beta^* = \beta_i^* [1 + \zeta^* F(M_t)] \quad (2.18)$$

$$\beta_i^* = \beta_\infty^* \left( \frac{\frac{4}{15} + (Re_t/R_\beta)^4}{1 + (Re_t/R_\beta)^4} \right), \zeta^* = 1.5, R_\beta = 8, \beta_\infty^* = 0.09 \quad (2.19)$$

$$\Omega_{ij} = \frac{1}{2} \left( \frac{\partial u_i}{\partial x_j} - \frac{\partial u_j}{\partial x_i} \right) \quad (2.20)$$

$$\beta = \beta_i [1 - \frac{\beta_i^*}{\beta_i} \zeta^* F(M_t)] \quad (2.21)$$

The turbulent eddy-viscosity is computed from :

$$\mu_t = \alpha^* \frac{\rho k}{\omega}, \alpha^* = \alpha_\infty^* \left( \frac{\alpha_0^* + Re_t/R_k}{1 + Re_t/R_k} \right), Re_t = \frac{\rho k}{\mu \omega}, R_k = 6, \alpha_0^* = \frac{\beta_i}{3} \quad (2.22)$$

where

$$\beta_i = F_1\beta_{i,1} + (1 - F_1)\beta_{i,2} \quad (2.23)$$

The blending function is :

$$F_1 = \tanh(\Phi_1^4), \Phi_1 = \min \left[ \max \left( \frac{\sqrt{k}}{0.09\omega y}, \frac{500\mu}{\rho y^2 \omega} \right), \frac{4\rho k}{\sigma_{\omega,2} D_{\omega}^+ y^2} \right] \quad (2.24)$$

where

$$D_{\omega}^+ = \max \left[ 2\rho \frac{1}{\sigma_{\omega,2}} \frac{1}{\omega} \frac{\partial k}{\partial x_j} \frac{\partial \omega}{\partial x_j}, 10^{-10} \right] \quad (2.25)$$

If compressibility correction is applied, from Eq. (2.18) and Eq. (2.21)

$$F(M_t) = \begin{cases} 0 & M_t \leq M_{t0} \\ M_t^2 - M_{t0}^2 & M_t > M_{t0} \end{cases} \quad (2.26)$$

where

$$M_t^2 \equiv \frac{k}{a^2}, M_{t0} = 0.25, a = \sqrt{\gamma RT} \quad (2.27)$$

The model constants are given in [17].

### 2.1.3 Shear-Stress Transport (SST) $k$ - $\omega$ model

SST  $k$ - $\omega$  turbulence model is one of the two-equation eddy viscosity models combining the characteristics of the  $k$ - $\omega$  and  $k$ - $\varepsilon$  turbulence models. It has been widely used for flows such as adverse pressure gradient flows, airfoils, transonic shock waves and other external flows. Near wall boundaries, it behaves like a regular  $k$ - $\omega$  model directly integrable to the wall. But its behavior changes to the  $k$ - $\varepsilon$  model in the free stream and shear layers. The full formulation of the model has been shown by Menter [17]. The following equations are the transport equations in Fluent with respect to Reynolds Averaged Navier-Stokes (RANS) equations.

$$\frac{D}{Dt}(\rho k) = \frac{\partial}{\partial x_j} \left[ \left( \mu + \frac{\mu_t}{\sigma_k} \right) \frac{\partial k}{\partial x_j} \right] - \rho \overline{u'_i u'_j} \frac{\partial u_j}{\partial x_i} - \rho \beta^* k \omega \quad (2.28)$$



$$\frac{D}{Dt}(\rho\omega) = \frac{\partial}{\partial x_j} \left[ \left( \mu + \frac{\mu_t}{\sigma_\omega} \right) \frac{\partial \omega}{\partial x_j} \right] - \frac{\alpha\alpha^*}{\nu_t} \overline{\rho u'_i u'_j} \frac{\partial u_j}{\partial x_i} - \rho\beta\omega^2 + 2(1 - F_1)\rho \frac{1}{\omega\sigma_{\omega,2}} \frac{\partial k}{\partial x_j} \frac{\partial \omega}{\partial x_j} \quad (2.29)$$

$\alpha$ ,  $\alpha^*$  are shown Eq. (2.17) and Eq. (2.22). The blending function  $F_1$  is the same as Eq. (2.24) above.

The turbulent eddy-viscosity is computed from :

$$\mu_t = \frac{\rho k}{\omega} \frac{1}{\max \left[ \frac{1}{\alpha^*}, \frac{SF_2}{\alpha_1 \omega} \right]}, S = \sqrt{2S_{ij}S_{ij}}, S_{ij} = \frac{1}{2} \left( \frac{\partial u_j}{\partial x_i} + \frac{\partial u_i}{\partial x_j} \right) \quad (2.30)$$

$$F_2 = \tanh(\Phi_2^2), \Phi_2 = \max \left[ 2 \frac{\sqrt{k}}{900\omega y}, \frac{500\mu}{\rho y^2 \omega} \right] \quad (2.31)$$

As for compressibility correction of SST model is applied in same manner as BSL model.

The model constants are given in [17].

#### 2.1.4 Realizable $k$ - $\varepsilon$ model

The realizable  $k$ - $\varepsilon$  model contains an alternative formulation for the turbulent viscosity. A modified transport equation for the dissipation rate,  $\varepsilon$ , has been derived from an exact equation for the transport of the mean-square vorticity fluctuation. The realizable  $k$ - $\varepsilon$  model proposed by Shih et al. [18] was intended to solve some deficiencies of traditional  $k$ - $\varepsilon$  models. The following equation is the transport equation in Fluent in conjunction with RANS equations [15].

$$\frac{\partial}{\partial t}(\rho k) + \frac{\partial}{\partial x_j}(\rho k u_j) = \frac{\partial}{\partial x_j} \left[ \left( \mu + \frac{\mu_t}{\sigma_k} \right) \frac{\partial k}{\partial x_j} \right] - \overline{\rho u'_i u'_j} \frac{\partial u_j}{\partial x_i} - \rho\varepsilon \quad (2.32)$$

$$\frac{\partial}{\partial t}(\rho\varepsilon) + \frac{\partial}{\partial x_j}(\rho\varepsilon u_j) = \frac{\partial}{\partial x_j} \left[ \left( \mu + \frac{\mu_t}{\sigma_\varepsilon} \right) \frac{\partial \varepsilon}{\partial x_j} \right] + \rho C_1 S \varepsilon - \rho C_2 \frac{\varepsilon^2}{k + \sqrt{\nu \varepsilon}} \quad (2.33)$$

where

$$C_1 = \max \left[ 0.43, \frac{\eta}{\eta + 5} \right], \eta = S \frac{k}{\varepsilon}, S = \sqrt{2S_{ij}S_{ij}} \quad (2.34)$$

The eddy-viscosity is computed from :

$$\mu_t = \rho C_\mu \frac{k^2}{\varepsilon} \quad (2.35)$$

$C_\mu$  is no longer constant which is the difference from other traditional  $k$ - $\varepsilon$  models. It is computed from :

$$C_\mu = \frac{1}{A_0 + A_S \frac{kU^*}{\varepsilon}} \quad (2.36)$$

where

$$U^* \equiv \sqrt{S_{ij}S_{ij} + \tilde{\Omega}_{ij}\tilde{\Omega}_{ij}} \quad (2.76)$$

and

$$\tilde{\Omega}_{ij} = \Omega_{ij} - 2\varepsilon_{ijk}\omega_k, \Omega_{ij} = \bar{\Omega}_{ij} - \varepsilon_{ijk}\omega_k \quad (2.38)$$

where  $\bar{\Omega}_{ij}$  is the mean rate-of-rotation tensor viewed in a moving reference frame with the angular velocity  $\omega_k$ . The model constants  $A_0$  and  $A_S$  are given by

$$A_0 = 4.04, A_S = \sqrt{6} \cos \varphi \quad (2.39)$$

where

$$\varphi = \frac{1}{3} \cos^{-1}(\sqrt{6}W), W = \frac{S_{ij}S_{jk}S_{ki}}{\tilde{S}^3}, \tilde{S} = \sqrt{S_{ij}S_{ij}}, S_{ij} = \frac{1}{2} \left( \frac{\partial u_j}{\partial x_i} + \frac{\partial u_i}{\partial x_j} \right) \quad (2.40)$$

On the other hand, the dilatation dissipation term was added to  $k$  equation of  $k$ - $\varepsilon$  model Eq. (2.32). The term which was added is :

$$2\rho\varepsilon M_t^2 \quad (2.41)$$

where

$$M_t = \sqrt{\frac{k}{a^2}} \quad (2.42)$$

The model constants are given in [15]

## 2.2 Discretization Schemes

### 2.2.1 Third-Order MUSCL Scheme

There are a lot of numerical schemes for the discretization of the convection-diffusion term in finite volume method (FVM). For example, central scheme, upwind scheme, hybrid scheme and QUICK are representative schemes. In the present work, third-order Monotone Upstream-Centered Schemes for Conservation Laws (MUSCL) scheme is used for the discretization. Firstly, the central-differencing scheme calculates the face value for a variable ( $\varphi_f$ ) as follows :

$$\varphi_{f,CD} = \frac{1}{2}(\varphi_0 + \varphi_1) + \frac{1}{2}(\nabla\varphi_0 \cdot \vec{r}_0 + \nabla\varphi_1 \cdot \vec{r}_1) \quad (2.43)$$

where the indices 0 and 1 refer to the cells that share face  $f$ ,  $\nabla\varphi_{r,0}$  and  $\nabla\varphi_{r,1}$  are the reconstructed gradients at cells 0 and 1, respectively, and  $\vec{r}$  is the vector directed from the cell centroid toward the face centroid. In order to avoid unbounded solutions and non-physical wiggles which can lead to stability problems for the numerical procedure by central-differencing schemes, a deferred correction is used for the central-differencing scheme. In Fluent, the face value is calculated as follows :

$$\varphi_f = \varphi_{f,UP} + (\varphi_{f,CD} - \varphi_{f,UP}) \quad (2.44)$$

where UP stands for upwind. The upwind part is treated implicitly while the difference between the central-difference and upwind values is treated explicitly. The third-order convection scheme was conceived from the original MUSCL [19] by blending a central differencing scheme and second-order upwind scheme as

$$\varphi_f = \theta\varphi_{f,CD} + (1 - \theta)\varphi_{f,SOU} \quad (2.45)$$

where  $\varphi_{f,CD}$  is defined in Eq. (2.43) and  $\varphi_{f,SOU}$  is computed using the second-order upwind scheme as

$$\varphi_{f,SOU} = \varphi + \nabla\varphi \cdot \vec{r} \quad (2.46)$$

The MUSCL scheme has some advantages. For instance, unlike the QUICK scheme, which

is applicable to structured hex meshes only in Fluent, the MUSCL scheme is applicable to arbitrary meshes. Compared to the second-order upwind scheme, the third-order MUSCL has a potential to improve spatial accuracy for all types of meshes by reducing numerical diffusion, most significantly for complex three-dimensional flows, and it is available for all transport equations.

### 2.2.2 Implicit Discretization Scheme

There are two methods of discretization for the rate of change term. One is the Explicit method and the other is the Implicit method. Each method has advantages and disadvantages. First of all, Explicit scheme has the advantage to write code easily because of its simplicity.

But it has a stability problem. Therefore the time step size is limited, which induces long computation time. If the higher dimension is considered, the more strict stability criteria are needed for satisfactory results. In addition to the stability problems, the time lag occurs at boundary conditions.

**Table 2.** *The advantages and disadvantages of the explicit scheme and implicit scheme*

	<b>Advantages</b>	<b>Disadvantages</b>
<b>Explicit Scheme</b>	<ul style="list-style-type: none"> <li>• Easy to write code compared to implicit scheme</li> </ul>	<ul style="list-style-type: none"> <li>• Limited time step size due to a stability problem</li> <li>• If the higher dimension is considered, the more strict stability criteria are necessary</li> <li>• Time lag at boundary condition</li> </ul>
<b>Implicit Scheme</b>	<ul style="list-style-type: none"> <li>• Unconditionally stable</li> </ul>	<ul style="list-style-type: none"> <li>• Difficult to write code</li> <li>• Require more time than explicit scheme for one time step</li> </ul>

On the other hand, the Implicit scheme is unconditionally stable. This is a reason why it solves the matrix equation at every time step. It takes more time to solve the one time step than the explicit scheme takes. However, considering total computation time, the implicit scheme takes shorter than the explicit scheme, which means the solution converges with a large time step size. But if the time step size is too large, the truncation error contaminates the solution. Table.1 shows the advantages and disadvantages of the explicit scheme and implicit scheme.

### 2.2.3 Flux type

In order to compute the flux vector, flux-vector splitting scheme is used [20]. The scheme, is called Advection Upstream Splitting Method (AUSM), was introduced by Liou and Steffen [21]. Firstly, the AUSM scheme computes a cell interface Mach number based on the characteristic speeds from the neighboring cells. The interface Mach number is then used to determine the upwind extrapolation for the convection part of the inviscid fluxes. A separate Mach number splitting is used for the pressure terms. Generalized Mach number based convection and pressure splitting functions were proposed by Liou [22] and the new scheme was called AUSM+ which is used in this work. The AUSM+ scheme has several desirable properties providing exact resolution of contact and shock discontinuities, preserving positivity of scalar quantities, and free of oscillations at stationary and moving shocks [23]. The AUSM+ scheme avoids using an explicit artificial dissipation, by proposing a numerical flux of the form :

$$F = m_f \varphi + p_i \quad (2.47)$$

$m_f$  is the mass flux through the interface, which is computed using the fourth order polynomial functions of the left and right side of the interface Mach numbers.

## **Chapter 3. Theoretical Background for Uncertainty Quantification**

### **3.1 The Definition of Uncertainty Quantification**

The uncertainty quantification is the mathematical method that deals with quantitative characterization and the reduction of uncertainties in applications. Uncertainty quantification is used for robust design/optimization, model validation, and certification for high-risk decisions.

Uncertainty means that there is not certain value for a specific parameter because of the physical variation of the value and the lack of accuracy in calculation and measurement. There are two categories to classify the type of uncertainty. The one is aleatory uncertainty and the other one is epistemic uncertainty. Aleatory uncertainty is induced by natural variabilities in the real system. Therefore it is impossible to be reduced or eliminated. For examples of aleatory uncertainty, there are material properties, noise, etc. Epistemic uncertainty is induced by the lack of knowledge of physics and it is caused by the modeling hypothesis. Hence, it is possible to be reduced or eliminated. For instance, there are turbulence models, boundary conditions etc.

Research incorporating UQ has been investigated by many researchers. Huan et al. [24] conducted global sensitivity analysis to identify influential input parameters, which are inflow, fuel inflow, and wall boundary condition, and turbulence model parameters in scramjet computations by using UQ. Also, estimation of model error concerning models of different fidelity was investigated. Burt and Josyula [25] considered aleatory and epistemic uncertainties in sensitivity analysis/uncertainty quantification calculations. Global sensitivity analysis and uncertainty quantification are integrated with a direct simulation which is Monte Carlo gas flow simulation code for a hypersonic double-cone flow.

In this thesis, entire process of UQ is conducted by UQLab framework [26] using MATLAB [27].

### **3.2 Polynomial Chaos Expansions**

The Polynomial chaos expansions (PCE) is non-intrusive method to determine propagation of uncertainty in dynamic system when there is probabilistic uncertainty in the system parameters. It allows one to represent a random output as a polynomial series in the input variables. The generic problem can be described like below :

$$y = f(x) \quad (3.1)$$

$f$  is the computational model and in the present research, it is the Navier-Stokes equation.  $x$  is the input parameter.  $y$  is the output referred to Quantity of interest (QOI). As input parameter  $x$  is a random variable, the equation is modified like below :

$$Y = f(X) \quad (3.2)$$

$Y$  and  $X$  are expressed as random variables. If the assumption that the output random variable has finite variance is applied, the Eq. (3.2) is modified as follow :

$$Y = \sum_{n=0}^{\infty} \alpha_n(X) \Psi_n(\xi_j) \quad j = 0, 1, 2, \dots, P \quad (3.3)$$

Where  $\alpha_n(X)$  are the polynomial chaos coefficients and  $\Psi_n$  is an element of an orthogonal family. This correspondences between the random variable distribution and orthogonal polynomial family are shown in Table.2.

**Table 3.** Classical families of orthogonal polynomials

Type of variable	Distribution	Orthogonal polynomials	Hilbertian basis $\Psi_n(\xi)$
Uniform $U(-1,1)$	$\frac{1(\xi)}{2}$	Legendre $P_n(\xi)$	$P_n(\xi) / \sqrt{\frac{1}{2n+1}}$
Gaussian $G(0,1)$	$\frac{1}{\sqrt{2\pi}} e^{-\xi^2/2}$	Hermite $H_n(\xi)$	$H_n(\xi) / \sqrt{n!}$
Gamma $\Gamma(a, \lambda = 1)$	$x^a e^{-\xi}$	Laguerre $L_n^a(\xi)$	$L_n^a(\xi) / \sqrt{\frac{\Gamma(n+a+1)}{n!}}$
Beta $B(a, b)$	$1(\xi) \frac{(1-\xi)^a (1+\xi)^b}{B(a)B(b)}$	Jacobi $J_n^{a,b}(\xi)$	$J_n^{a,b}(\xi) / \mathfrak{A}_{a,b,n}$

$\xi$  are a vector of random variables representing the system's uncertainties. the random variable  $\xi$  is randomly sampled in accordance with its statistical distribution equation above represents a system of  $P + 1$  equations in  $P + 1$  unknowns. As a system of linear equations, the Eq. (3.3) can be solved for the  $\alpha_n$ . A linear system can be obtained as follow :

$$\begin{bmatrix} \Psi_0(\xi_0) & \Psi_0(\xi_0) & \dots & \Psi_P(\xi_0) \\ \Psi_0(\xi_1) & \Psi_0(\xi_1) & \dots & \Psi_P(\xi_1) \\ \vdots & \vdots & \ddots & \vdots \\ \Psi_0(\xi_{P-1}) & \Psi_1(\xi_{P-1}) & \dots & \Psi_P(\xi_{P-1}) \\ \Psi_0(\xi_P) & \Psi_1(\xi_P) & \dots & \Psi_P(\xi_P) \end{bmatrix} \begin{bmatrix} \alpha_0 \\ \alpha_1 \\ \vdots \\ \alpha_{P-1} \\ \alpha_P \end{bmatrix} = \begin{bmatrix} Y_1 \\ Y_2 \\ \vdots \\ Y_{P-1} \\ Y_P \end{bmatrix} \quad (3.4)$$

If the more than  $P + 1$  samples are chosen, then the over-determined system of equations should be solved using the least square method.

The maximum number of terms,  $P + 1$ , may be computed from the formula

$$P + 1 = \frac{(p + n)!}{p! n!} \quad (3.5)$$

where  $p$  is the order of the polynomial set used for the chaos. If the order from Eq. (3.5) is decided, it means the number of coefficients is also decided, which should be calculated. This is calculated by two methods. One of the methods is called “projection method” and another one is least-square minimization method. In this current work, least-square minimization method which has an advantage that an arbitrary number of points can be used to calculate the coefficients, as long as they are a representative sample of the random input vector, is adopted. Least-square minimization is a method that minimize a truncation error. Truncated PCE and a residual are expressed as :

$$Y = \mathcal{M}(\mathbf{X}) = \sum_{j=0}^{P-1} y_j \Psi_j(\mathbf{X}) + \varepsilon_P \equiv \mathbf{y}^T \Psi(\mathbf{X}) + \varepsilon_P \quad (3.6)$$

where  $P-1 =$  order of PCE,  $\varepsilon_P$  is the truncation error,  $\mathbf{y}_\alpha = \{y_0, \dots, y_{P-1}\}^T$  is a vector containing the coefficients and  $\Psi(x) = \{\Psi_0(x), \dots, \Psi_{P-1}(x)\}^T$  is the matrix that assembles the values of all the orthonormal polynomials in  $\mathbf{X}$ . The least-square minimization can be as :

$$\hat{\mathbf{y}} = \operatorname{argmin} \mathbb{E} \left[ (\mathbf{y}^T \Psi(\mathbf{X}) - \mathcal{M}(\mathbf{X}))^2 \right] \quad (3.7)$$



Eq. (3.7) is solved by ordinary least-squares (OLS). The ordinary least-square solution of Eq. (3.7) is:

$$\hat{\mathbf{y}} = (\mathbf{A}^T \mathbf{A})^{-1} \mathbf{A}^T \mathbf{y} \quad (3.8)$$

where

$$A_{ij} = \Psi_j(x^{(i)}) \quad i = 1, \dots, n \quad ; \quad j = 0, \dots, P - 1 \quad (3.9)$$

$\mathbf{y}$  is the model responses corresponding to input random vector.

There is a way to evaluate the error of constructed PCE, which is called the leave-one-out (LOO) cross-validation error. The leave-one-out cross-validation error ( $\epsilon_{LOO}$ ) is designed to overcome over-fitting limitation by using cross-validation. When the least-square minimization is used for calculating the coefficients, the formulation to calculate  $\epsilon_{LOO}$  is :

$$\epsilon_{LOO} = \sum_{i=1}^N \left( \frac{\mathcal{M}(x^{(i)}) - \mathcal{M}^{PC}(x^{(i)})}{1 - h_i} \right)^2 / \sum_{i=1}^N (\mathcal{M}(x^{(i)}) - \hat{\mu}_Y)^2 \quad (3.10)$$

where  $h_i$  is the  $i^{th}$  component of the vector, which is given like below:

$$\mathbf{h} = \text{diag}(\mathbf{A}(\mathbf{A}^T \mathbf{A})^{-1} \mathbf{A}^T) \quad (3.11)$$

And  $\mathbf{A}$  is the experimental matrix in Eq. (3.9).  $\mathcal{M}(x^{(i)})$  is the model response and  $\mathcal{M}^{PC}(x^{(i)})$  is the PCE result.  $\hat{\mu}_Y$  means the mean of the model response.

If a relationship between model responses and input parameters requires high-order, OLS could have too many terms, which means that it needs quite many input parameters depending on Eq. (3.5). In order to overcome this issue, in this thesis, least angle regression (LARS) which is starting from a small candidate polynomial basis, is used. Also, the results obtained by OLS and LARS are compared each other.

### 3.3 Sampling Method

Latin Hypercube Sampling (LHS) method is the one of the sampling method and it is proposed by McKay et al. [28]. LHS is developed to improve the computational efficiency

and the global accuracy of approximation. The key to this method is stratification of the input probability distribution. Stratification divides the cumulative curve into equal interval. A sample is then randomly taken from each interval or “stratification”.

Hosder et al. [29] investigated the effects on the results by the number of collocation points in a systematic way through the introduction of a parameter, the oversampling rate  $n_p$  defined below.

$$n_p = \frac{\text{the number of samples}}{P + 1} \quad (3.12)$$

Oversampling rate  $n_p = 2$  yields a better approximation to the statistic at each polynomial degree.

### 3.4 Surrogate Model

Deterministic solver is being gradually substituted by stochastic modelling to account for the inevitable uncertainty in physical phenomena and measurements. However, applying stochastic modeling is not an efficient way because it costs a lot of time. Surrogate modeling can offset the increased costs of stochastic modeling by substituting the expensive-to-evaluate computational models with inexpensive-to-evaluate surrogates. Also, QOIs prediction, QOIs distribution and sensitive analysis are able to be investigated through the surrogate model.

In this thesis, PCE which is a powerful metamodeling technique, is used to construct a surrogate model. PCE used for the current work is constructed based on the simulation results over compressible flows. The robustness of the surrogate model which is corresponding to the PCE order is evaluated by  $\epsilon_{LOO}$ . QOIs prediction and QOI distribution which are specified in this thesis can be known by using surrogate model. Also, which input parameter is dominant, is able to be studied through the surrogate model.

### 3.5 Bayesian Inference

As mentioned above, the normal way that input parameters are computed in a computational model to get the outputs is the forward problem. On the contrary, inverse problem is the process to get unknown parameters that cannot be measured directly are

estimated based on experiment data, which is indirectly associated with the parameters through a computational model. Inverse problem, because instead of propagating information about input variables through a computational model (Forward problem), the goal is to propagate information about the observations backwards to obtain insight on the model inputs. This inverse problem is able to obtain some results through the Bayesian inference which is based on bayes theorem. Formulation of bayes theorem is :

$$\pi(\theta|x) = \frac{\pi(x|\theta)\pi(\theta)}{\pi(x)} \quad (3.13)$$

where  $\pi(\theta)$  is the prior distribution about the input parameters. This could be set up heuristically or could be set up through a predetermined tendency.  $\pi(x|\theta)$  is the likelihood. Likelihood measures the suitable statistical model with respect to given data that consider observation and prior distribution.  $\pi(x)$  is a factor to normalize the right-hand side. As a result of this, posterior distribution is finally calculated.

### 3.6 Likelihood

Based on likelihood mentioned above, in case of independent observations given, the likelihood function is modeled as follows :

$$\mathcal{L}: \theta \rightarrow \mathcal{L}(\theta; \chi) \stackrel{\text{def}}{=} \prod_{k=1}^n \pi(x_k|\theta) \quad (3.14)$$

$$\pi(\theta|\chi) = \frac{\mathcal{L}(\theta; \chi)\pi(\theta)}{Z} \quad (3.15)$$

$$\mathcal{L}(x; y) = \prod_{i=1}^N \frac{1}{\sqrt{(2\pi)^{N_{out}} \det(\Sigma)}} \exp\left(-\frac{1}{2}(y_i - \mathcal{M}(x))^T \Sigma^{-1}(y_i - \mathcal{M}(x))\right) \quad (3.16)$$

If the independent observations are used, the likelihood function is expressed as a form of multiplication Eq. (3.14). In Eq. (3.16),  $y_i$  means observations and  $\mathcal{M}$  is a computational forward model and  $x$  is a set of input parameters. This discrepancy term  $\Sigma$  represents the effects of measurement error which is obtained from experimental references [1, 30-34].

### 3.7 Markov Chain Monte Carlo (MCMC)

Posterior distribution does not have a analytic solution in practice. One option spread widely to solve inverse problems relies upon MCMC simulations. MCMC simulation is like the states of the sample space where prior distribution is defined are linked like a chain. Markov chains can be uniquely defined by their transition probability  $\mathcal{K}(x^{(t+1)}|x^{(t)})$  from the step  $x^{(t)}$  of the chain at iteration  $t$  to the step  $x^{(t+1)}$  at the subsequent iteration  $t + 1$ . Then, the posterior is the invariant distribution of the Markov chain if the specified transition probability fulfils the detailed balance condition :

$$\pi(x^{(t)}|\mathcal{Y}) \mathcal{K}(x^{(t+1)}|x^{(t)}) = \pi(x^{(t+1)}|\mathcal{Y}) \mathcal{K}(x^{(t)}|x^{(t+1)}) \quad (3.17)$$

The samples suggested based on the equation (3.17) are accepted or rejected. It is decided by an acceptance probability and there are various methods to decide. A representative method is called metropolis-hastings algorithm (MH), an expression of it is following as :

$$\alpha(x^{(*)}, x^{(t)}) = \min \left\{ 1, \frac{\pi(x^{(*)}|\mathcal{Y})p(x^{(t)}|x^{(*)})}{\pi(x^{(t)}|\mathcal{Y})p(x^{(*)}|x^{(t)})} \right\} \quad (3.18)$$

At iteration  $t$  from the current point  $x^{(t)}$ , one then draws a candidate point  $x^{(*)}$  from a proposal distribution  $p(x^{(*)}|x^{(t)})$ . After that, if  $x^{(t+1)} = x^{(*)}$ , the candidate is accepted. Or else the candidate is rejected. ( $x^{(t+1)} = x^{(t)}$ )

If a correlation shown in the posterior distribution is strong between parameters, most of the MCMC algorithms result in poor convergence and so much tuning is needed to solve this issue. To overcome this, in this present work, Affine invariant ensemble algorithm (AIES) is adopted and performs 1500 steps and 300 parallel chains. The first half of the sample points generated by all chains are removed as burn-in. And then, post-processing is performed after burn-in.

## Chapter 4. Deterministic Simulations

### 4.1 Geometry

The base geometry is selected from Forsythe [2]. A cylinder diameter is 63.5 mm. The cylinder of length is set to  $8R$ , where  $R$  is the base radius. This cylinder of length was determined to match the experimental momentum thickness [2]. The outflow is located  $10R$  downstream, while the far-field boundary is at  $4.15R$  from the axis of symmetry.

In case of the 24-deg compression ramp, the geometry is adopted from Gerolymos et al. [14]. In order to simulate efficiently, the computational profile is computed on the inlet boundary condition which is explained in details at a boundary condition section. No-slip wall is placed on the top and bottom. The upper wall is located 0.2 m away from the bottom wall of the downstream section. The inlet is far off 0.2 m from the beginning of the 24-deg ramp which is 0.15 m long. Various frames were used in the compression ramp experimental setups [30, 31] for the profile measurements. The details of frames and specific locations where experimental data were measured are well explained in [14, 30, 31].

### 4.2 Mesh

Structured grid is generated by using Pointwise [35]. To resolve the turbulent boundary layer near the wall and satisfy the wall unit ( $y^+$ ) within 1.0 which is averaged in the computational domain, the first cell height is set to  $1e^{-6}$  (m). The total number of cells were 180,000 ( $600 \times 300$ ) with respect to the compression ramp case, while 37,370 cells ( $100 \times 75$  on the length of cylinder,  $149 \times 205$  on the downstream from the base) were generated for the base case. The grid system adopted in the present simulation is shown in Fig. 1 and Fig. 2.

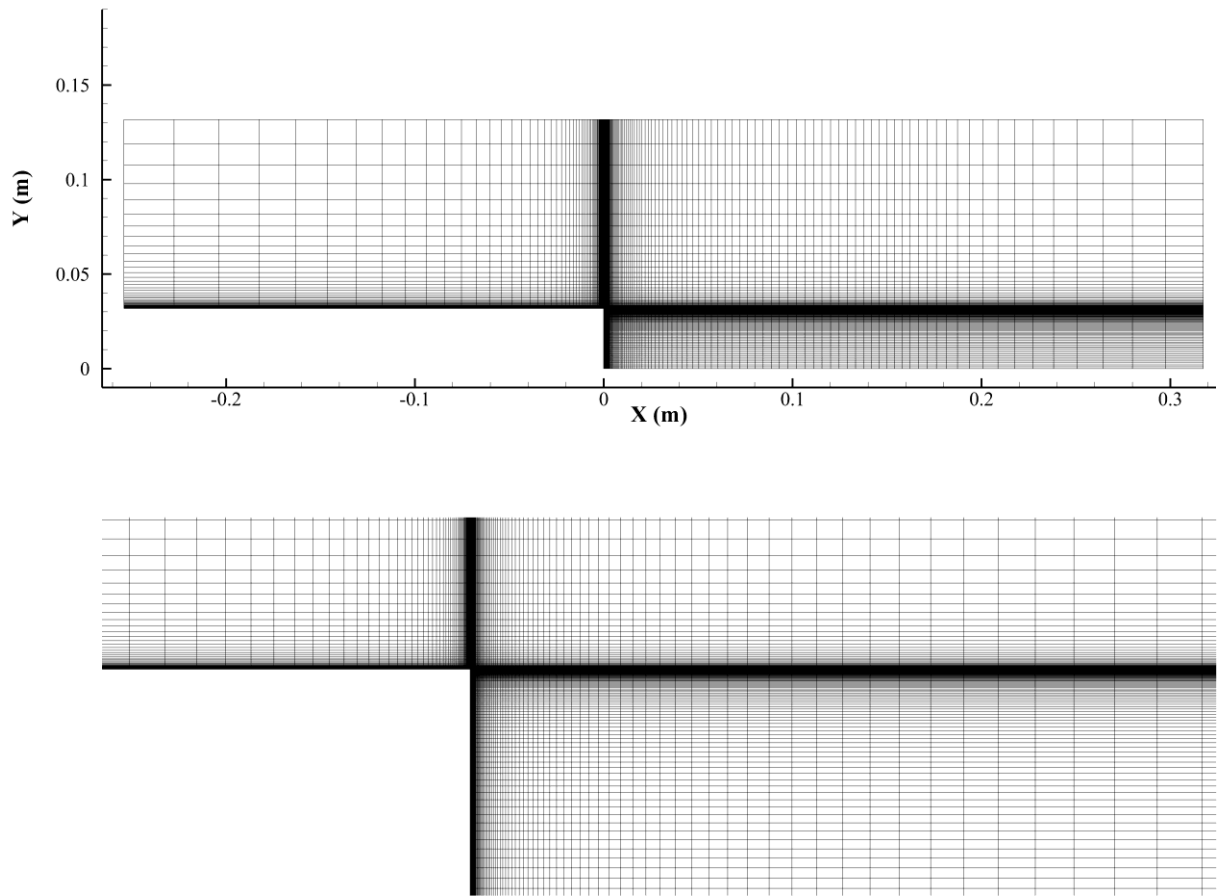


**Fig. 1.** Axisymmetric base flow computational grid, Closeup view of grid (bottom)

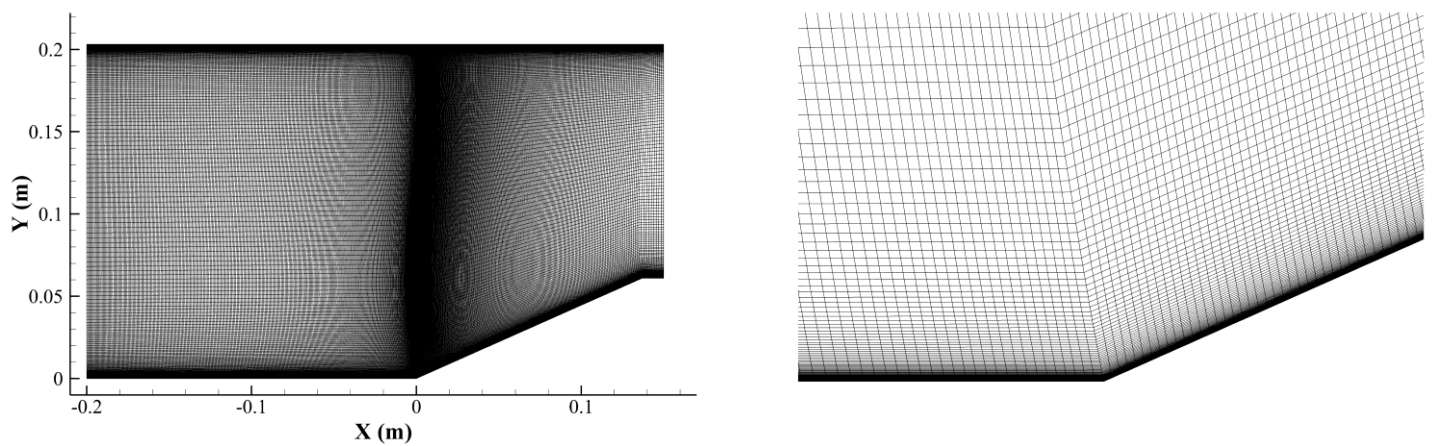


**Fig. 2.** 24-deg compression ramp computational grid (left), Closeup view of grid (right)

### 4.3 Boundary Conditions

In case of the compression ramp flow, at the upstream inlet boundary of the computational domain, profiles for all dependent variables such as  $k$ ,  $\varepsilon$  and  $\omega$  were specified. The profiles were obtained from a 2-D channel simulation. Supersonic inflow condition  $M_\infty=2.85$  was computed at the inlet boundary ( $Re_\infty=63 \times 10^6 \text{ m}^{-1}$ ). Wall temperature was fixed to  $T_w=258.8 \text{ K}$  in accordance with measurements [30, 32]. Extrapolation was applied at the downstream outlet boundary which was set to pressure outlet boundary condition.

On axisymmetric base flow, the experimental conditions of the axisymmetric base of Herrin and Dutton [1] were matched in this computation. Freestream conditions of  $M_\infty=2.46$  and a unit Reynolds number of  $45 \times 10^6$  per meter were computed at the inlet boundary. Adiabatic wall condition was used on the wall and the extrapolation was applied at the pressure outlet boundary as well. Fig. 3 shows the boundary conditions of each case.

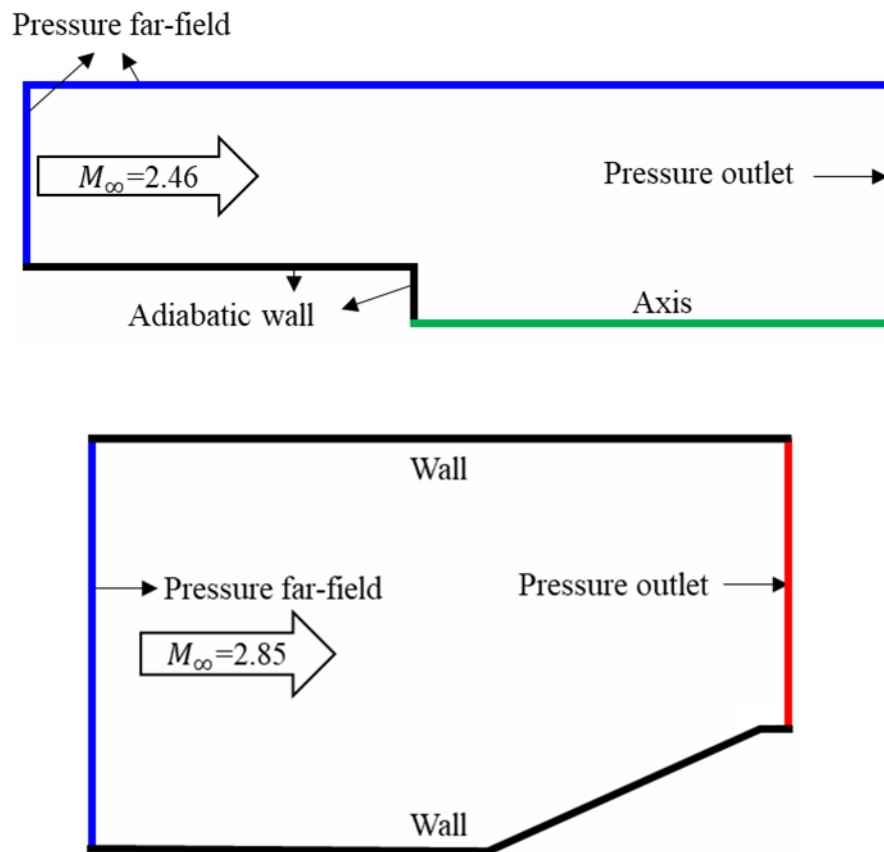


**Fig. 3** Boundary Conditions (Base flow : up, Ramp flow : bottom)

## 4.4 Results

### 4.4.1 Grid test

The grid test obtained by the GEKO model, is investigated by using tiny, coarse, medium, fine and extra fine mesh which are shown in Table 4, Table 5, Fig. 3 and Fig. 5. To evaluate the grid test, in this thesis, Reattachment Point (RP) and Pressure Coefficient on the base ( $C_{P_{base}}$ ) are used for axisymmetric base flow. On 24deg compression ramp, Reattachment Point (RP) and Separation Point (SP) are used. These are quantities of interest (QOIs) which are not only for the way to determine the grid test but also for UQ. To clarify  $C_{P_{base}}$  which is defined as Eq. (4.1), area-weighted average of the static pressure across the base surface is extracted to determine an average base pressure coefficient. RP and SP are determined based on wall shear stress data.

$$C_{P_{base}} = \frac{2[(P_{base} - P_{\infty}) - 1]}{\gamma M_{\infty}^2} \quad (4.1)$$

Grid convergence index (GCI) was devised by Roache [36, 37] to provide a measure of the computation's accuracy. There are several improved GCI methods. Modified GCI method from Roache's GCI [38, 39] was introduced in the ASME guideline [40]. The other one developed by Eça and Hoekstra [41] is called simplified least-square version GCI estimation method (SLS-GCI). In this work, total two GCI methods are used. One was introduced in the ASME guideline (Mod-ASME) and the other one is developed by Eça et al. [42] (SLS-GCI). Results obtained by GCI consist of 3 components to explain grid independency. First, extrapolation values which mean an estimate of the value of the each QOI at zero grid spacing, are shown (Table 8). Second,  $U_g$  is a measure of the computed value is away from the value of the asymptotic numerical value. It is estimated by the root mean square function with respect to the local GCI of  $u_g$ , which means local values [42]. It is determined by using fine grids among 3 grids (e.g. coarse and medium among tiny, coarse and medium grid). It indicates an error band on how far the solution is from the asymptotic value. It also indicates how much the solution would change with a further refinement of the grid. Thus, a small value indicates that the computation is within the asymptotic range. Hence,  $U_g$  indicates that the grids are reasonably generated if its value is close to zero (Table 6). Third,  $U_e$  which is calculated only in SLS-GCI presents the local error of estimation, which means the difference between numerical and estimated results



(Table 7).

**Table 4.** Grid independence test (Axisymmetric base flow)

	Tiny	Coarse	Medium	Fine	Extra fine
Number of cells	9,186	18,512	37,370	75,180	151,533
RP (m)	0.10181	0.10389	0.10549	0.10565	0.10575
$C_{p_{base}}$	-0.11263	-0.11006	-0.10867	-0.10807	-0.10789

**Table 5.** Grid independence test (24-deg compression ramp)

	Tiny	Coarse	Medium	Fine	Extra fine
Number of cells	45,000	90,100	180,000	358,700	720,000
RP (m)	0.062708	0.06395	0.064796	0.065475	0.065787
SP	-0.09465	-0.09808	-0.1007	-0.10292	-0.10411

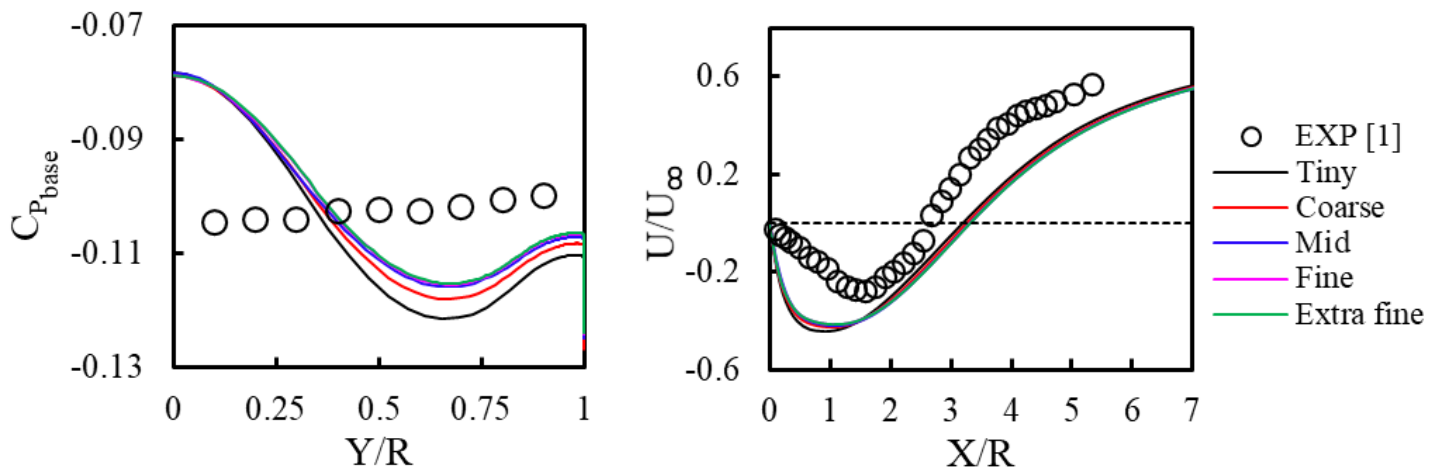


**Fig. 4.** Grid sensitivity test for base flow

Pressure distribution (left), Centerline velocity (right)

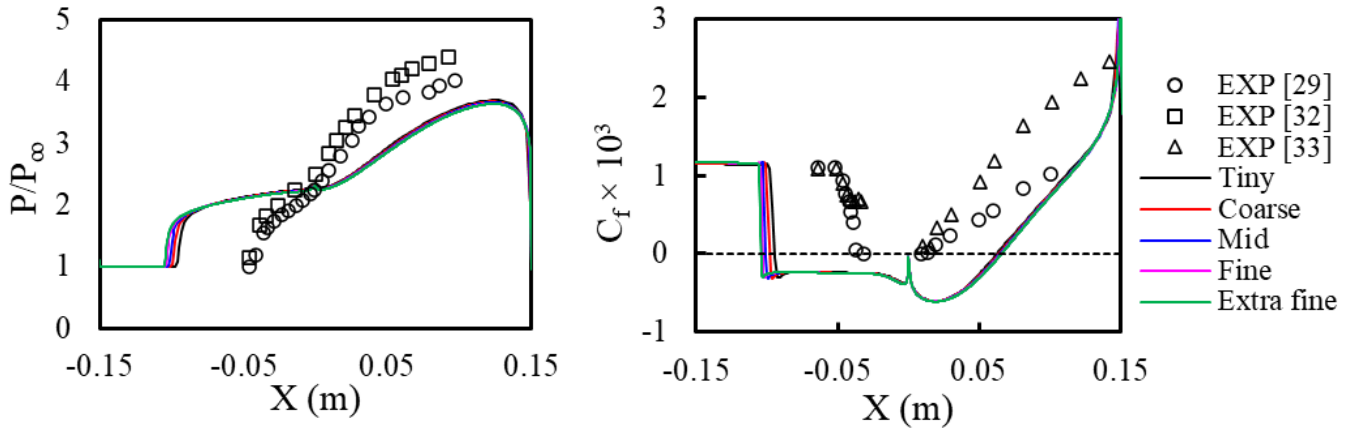


**Fig. 5.** Grid sensitivity test for compression ramp flow  
Nondimensional pressure distribution (left), Skin friction coefficient distribution (right)

**Table 6.**  $GCI U_g$  values

$U_g$		Mod_ASME				SLS-GCI			
		(1,2,3)	(2,3,4)	(3,4,5)	(1,3,5)	(1,2,3)	(2,3,4)	(3,4,5)	(1,3,5)
R A M P	RP	2.544E-03	2.051E-03	3.291E-04	9.910E-04	8.569E-04	6.242E-04	4.147E-04	2.458E-04
	SP	7.887E-03	6.705E-03	3.545E-03	3.409E-03	2.467E-03	1.977E-03	1.416E-03	7.447E-04
B A S E	RP	4.716E-03	5.177E-05	2.967E-04	2.436E-05	1.467E-03	7.552E-04	1.044E-04	3.321E-04
	$C_{P_{base}}$	4.101E-03	5.819E-04	9.525E-05	2.422E-04	1.607E-03	8.202E-04	3.278E-04	3.871E-04

**Table 7.**  $GCI U_e$  values

$U_e$		SLS-GCI			
		(1,2,3)	(2,3,4)	(3,4,5)	(1,3,5)
R A M P	RP	1.813E-03	1.315E-03	8.783E-04	1.876E-03
	SP	5.221E-03	4.166E-03	3.000E-03	5.681E-03
B A S E	RP	3.150E-03	1.619E-03	2.236E-04	2.611E-03
	$C_{P_{base}}$	3.453E-03	1.758E-03	7.022E-04	3.042E-03

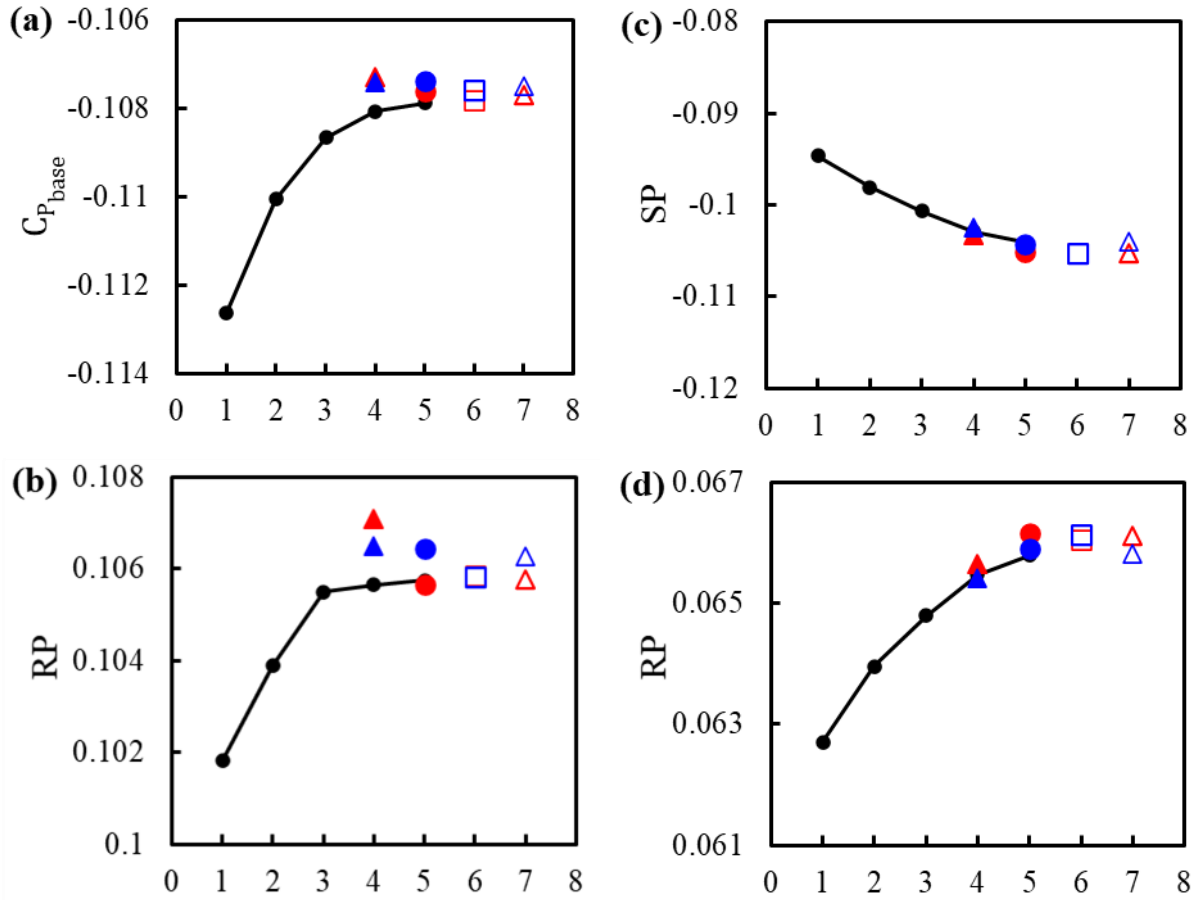


**Fig. 6.** Extrapolation values from GCI w.r.t QOIs. Base flow(a, b), Compression ramp flow(c, d)

Red (Mod\_ASME), Blue (SLS-GCI), filled triangle (1,2,3), circle (2,3,4), square (3,4,5), empty triangle (1,3,5)

**Table 8.** Extrapolation values from GCI

		Mod_ASME				SLS-GCI				Grid test
		(1,2,3)	(2,3,4)	(3,4,5)	(1,3,5)	(1,2,3)	(2,3,4)	(3,4,5)	(1,3,5)	Medium mesh
R	RP (m)	0.0656	0.0662	0.0661	0.0661	0.0654	0.0659	0.0661	0.0658	0.0648
A		(1.309)	(2.102)	(1.936)	(2.039)	(0.957)	(1.705)	(2.055)	(1.557)	
M	SP (m)	-0.1033	-0.1052	-0.1053	-0.1052	-0.1024	-0.1042	-0.1052	-0.1040	-0.1007
P		(2.611)	(4.423)	(4.558)	(4.514)	(1.699)	(3.515)	(4.491)	(3.258)	
B	RP (m)	0.1071	0.1057	0.1058	0.1058	0.1065	0.1064	0.1058	0.1063	0.1055
A		(1.490)	(0.166)	(0.339)	(0.263)	(0.957)	(0.896)	(0.318)	(0.731)	
S	Cp <sub>base</sub>	-0.1073	-0.1076	-0.1078	-0.1077	-0.1074	-0.1074	-0.1076	-0.1075	-0.1087
E		(1.258)	(0.984)	(0.792)	(0.900)	(1.153)	(1.182)	(0.995)	(1.073)	

Table 8, Fig. 6 show extrapolation values from GCI with respect to the QOIs. The values inside a bracket in Table 8 mean the error (%) between each extrapolation value and result of medium mesh. Combination (1,3,5) has the biggest spacing ratio but difference

from the result of medium mesh is less than 5 % (Max 4.5%). Hence, the medium mesh is selected for a computational domain.

#### 4.4.2 Base Flow

In case of the base flow, the velocity profile was obtained 1 mm upstream of the base corner. Fig. 7 shows that the velocity profiles are compared with the profile obtained from the experiment. Whether compressibility correction is used or not, the profiles of all models appear in a similar shape. Overall, all models predicted the boundary-layer profile reasonably well under the current mesh.

Fig. 8 shows pressure distributions along the base surface. The base pressure distributions obtained without the compressibility correction are quite lower compared to the experiment data [1]. On the other hand, the models that the compressibility correction was included show higher base pressure distributions but appear with enhanced variations along the base surface. Qualitative flat pressure distribution along the base surface is not predicted at all, when it comes to RANS models [2-7]. The reverse flow near the wake axis stagnates at the center of the base surface where the relatively high pressure appears (see Fig. 8, 10)

Fig. 9 shows static pressure after the base. Both contours are obtained from GEKO model but upper one is the result with compressibility correction and bottom one is the result without compressibility correction. It clearly shows that the pressure of GEKO-CC

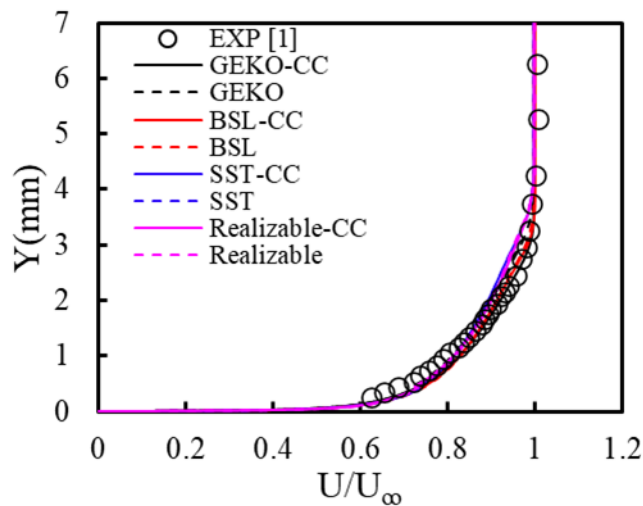


**Fig. 7.** Velocity profiles at 1 mm upstream from base edge.

around a centerline is higher than GEKO model, which is why the models with

compressibility correction show higher pressure than the models without the correction. Also, expansion fan and reattachment shock are observed. GEKO-CC model predicts slightly delayed high pressure region and reattachment shock than GEKO model.

One of the QOIs for axisymmetric base flow is the shear layer reattachment point. Fig. 10 shows the axial velocity along the axis. It is clearly shown that results from the models without compressibility correction match well the experiment data, when it comes to the reattachment point. If a smaller recirculation region as the models without compressibility

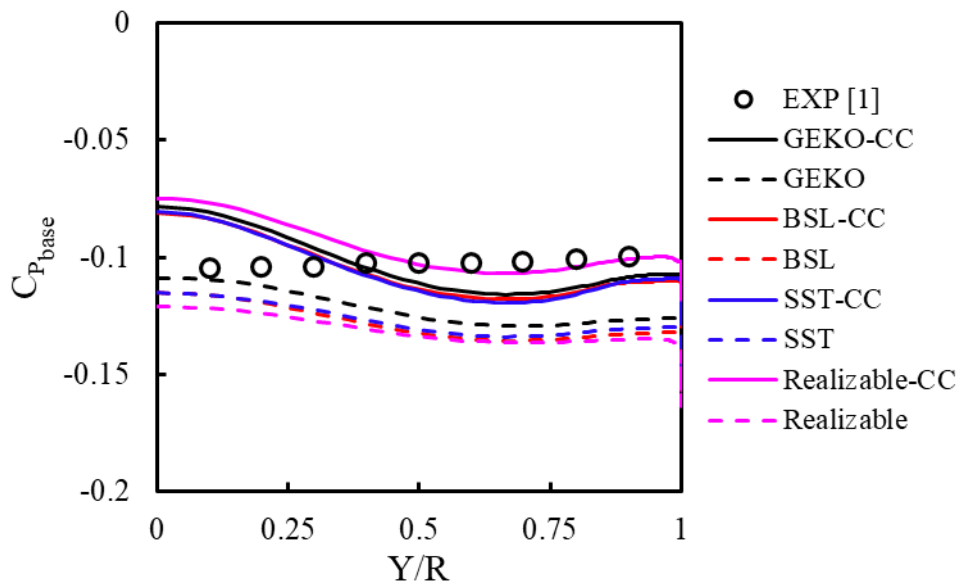


**Fig. 8.** Pressure distributions along base radius

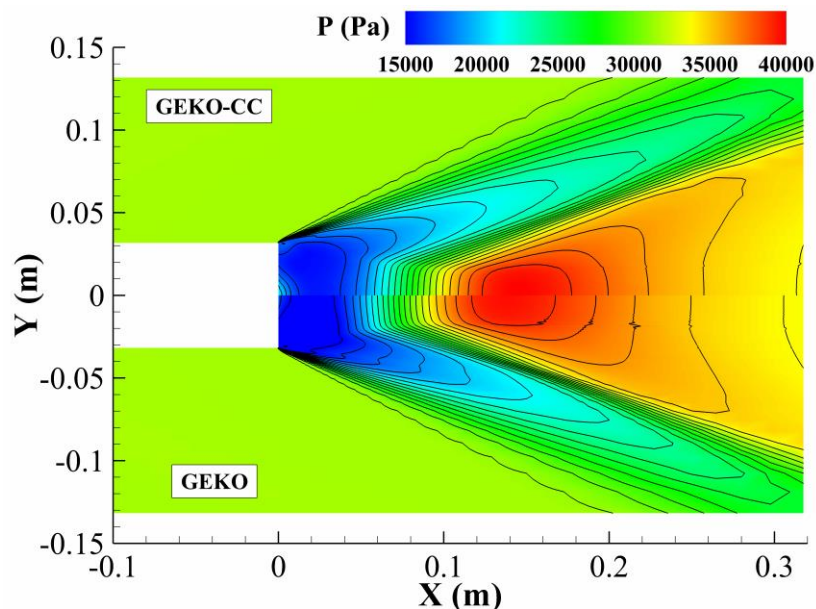


**Fig. 9.** Static pressure contour (GEKO-CC : up, GEKO : down)

correction predict is predicted, it causes the flow to turn sharply behind the base, leading to a more enhanced expansion wave, and the reduction in pressure. Small separation regions, therefore, cause larger pressure drag than large separated regions cause [2]. Models applied with compressibility correction overpredicted the peak reverse velocity more than measured data near the base surface. They overpredict not only the reattachment point but also the reverse velocity. When the reverse flow is overpredicted, the flow is more accelerated outward along the base radius, which can cause the pressure to decrease. This is a typical issue that RANS models cannot predict a flat pressure distribution along the base surface because of the large turbulent eddy viscosity [4].

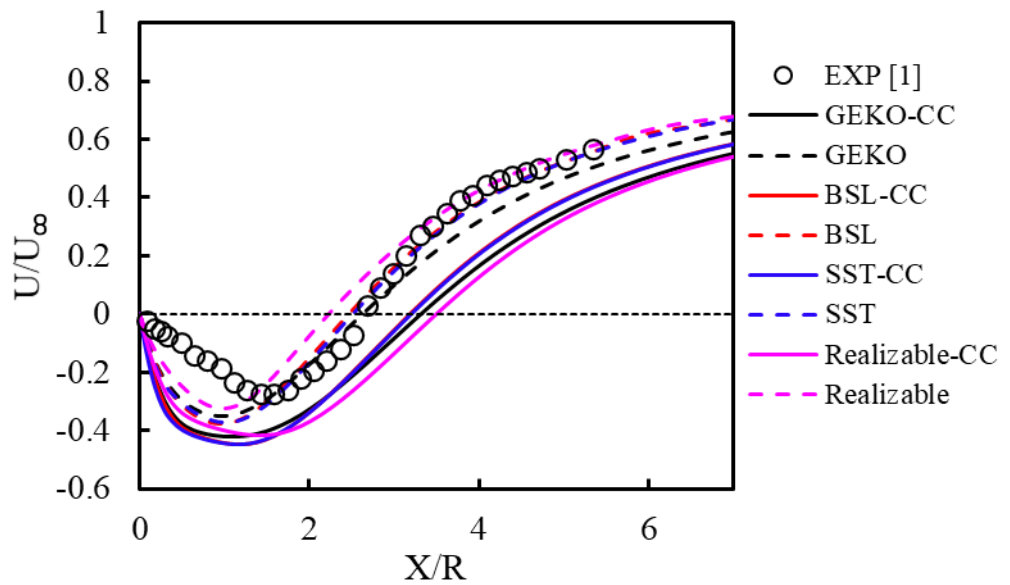


**Fig. 10.** Centerline velocity

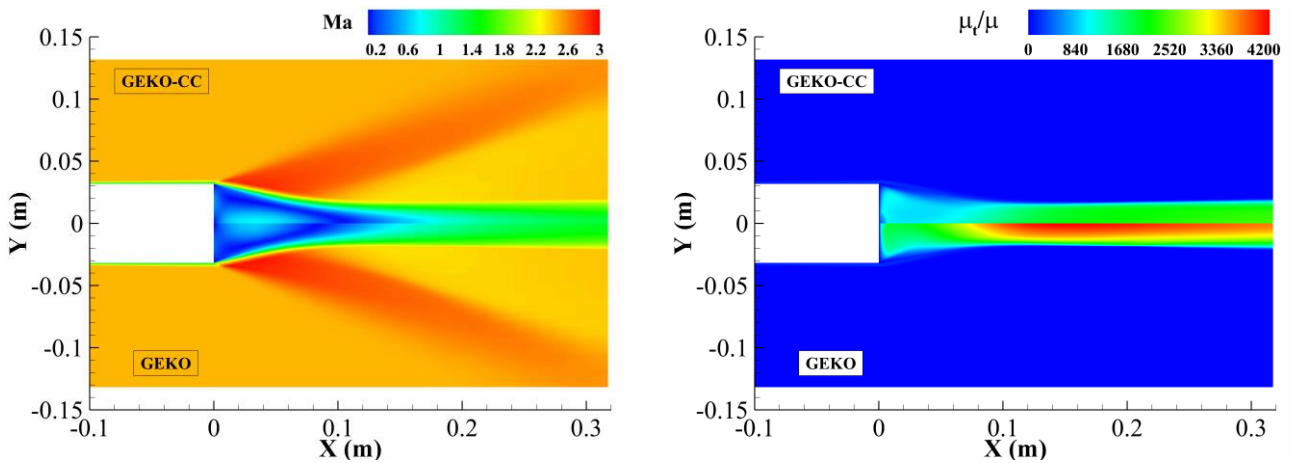


**Fig. 11.** Mach number (left) and turbulent viscosity ratio (right) contour

Mach number and turbulent viscosity ratio are shown in Fig. 11. Upper part of the figure is GEKO-CC and It is clearly seen that GEKO-CC model predicts RP further off than GEKO model from the base. As mentioned in introduction, compressibility correction reduces turbulent eddy viscosity, which can lead to higher pressure levels, but also it increases the reattachment length. Thus, the size/length of recirculation region behind the base is influenced depending on overpredicting or underpredicting the turbulent eddy viscosity. This factor can also be controlled by  $C_{SEP}$  coefficient of GEKO model, and it is indirectly indicated through turbulent viscosity ratio contour (Fig. 11) that how big influence  $C_{SEP}$  has. The facts depending on applying compressibility correction or not, about overpredicted and/or underpredicted the reattachment point, have also been shown by many researchers [2-7].

#### 4.4.3 24-deg Compression Ramp

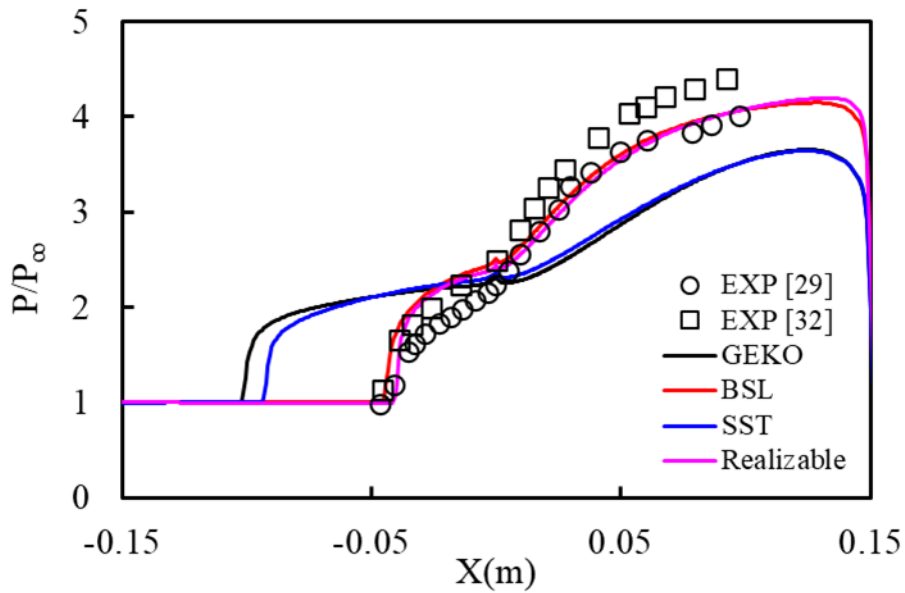
For 24-deg compression ramp case, the inlet profile including all dependent variables is computed at inlet. Boundary layer thickness ( $\delta$ ), displacement thickness ( $\delta^*$ ) and momentum thickness ( $\theta$ ) of the results obtained from the models (BSL, SST, Realizable model) are shown in Table 9. The profiles are extracted at a position where the profile were measured in the experiment [31]. SST model predict relatively lower  $\delta$  than other models do.

Fig. 12 shows nondimensional pressure distributions along bottom surface of the computational domain in 24deg compression ramp. To compare computational results, experiment data obtained from [30, 33, 34] were used. (The experiment data was found in

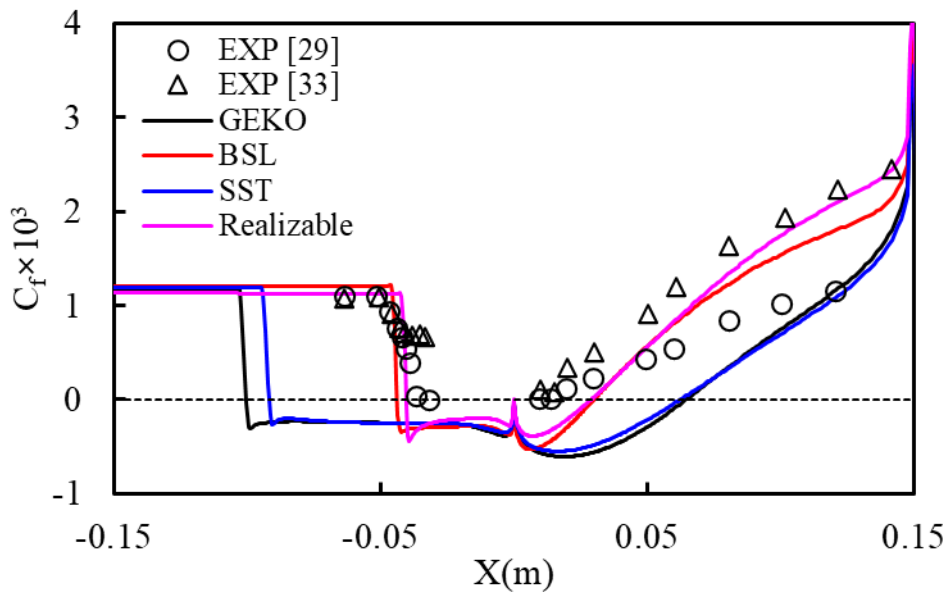
**Table 9.** *Boundary layer thickness*

Unit (mm)			
Model	$\delta$	$\delta^*$	$\theta$
BSL	22.555	6.017	1.497
SST	18.835	5.774	1.342
Realizable	21.581	5.272	1.280
EXP	21.082	6.020	1.143

[34], but exact source is not given. [14]) The result of GEKO model is quite similar with the result obtained from SST model as indicated [16]. Both models show overpredicted the length of the reversed flow region, which means that a separation shock occurs too early. The models under-predicted even lower pressure compared to the experiment data after the corner. BSL and Realizable model performed the best results in the pressure distribution. The initial pressure rise of the results obtained from both models matches the measured rise. This means that the separation shock predicted from numerical flowfields occurs in the same location as the experimental flowfields.



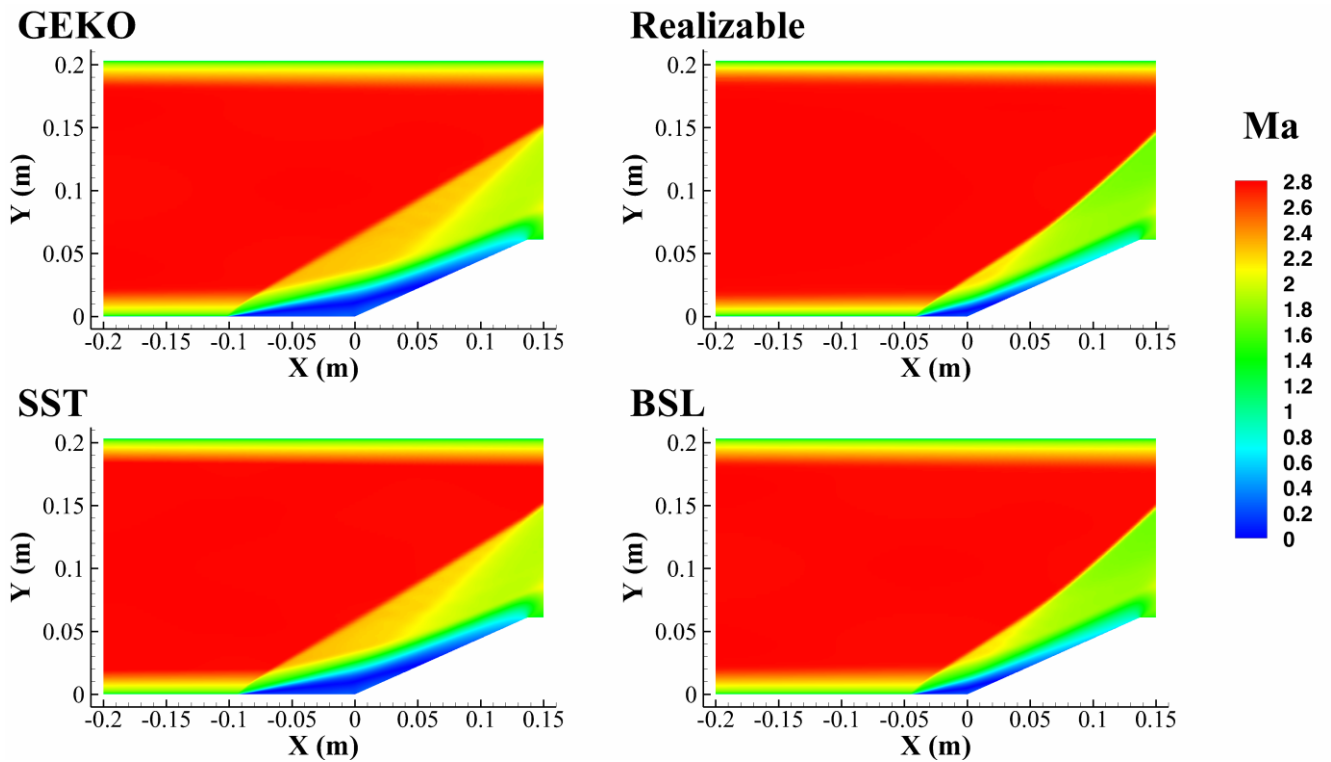
**Fig. 12.** *Nondimensional pressure distribution along the bottom surface*



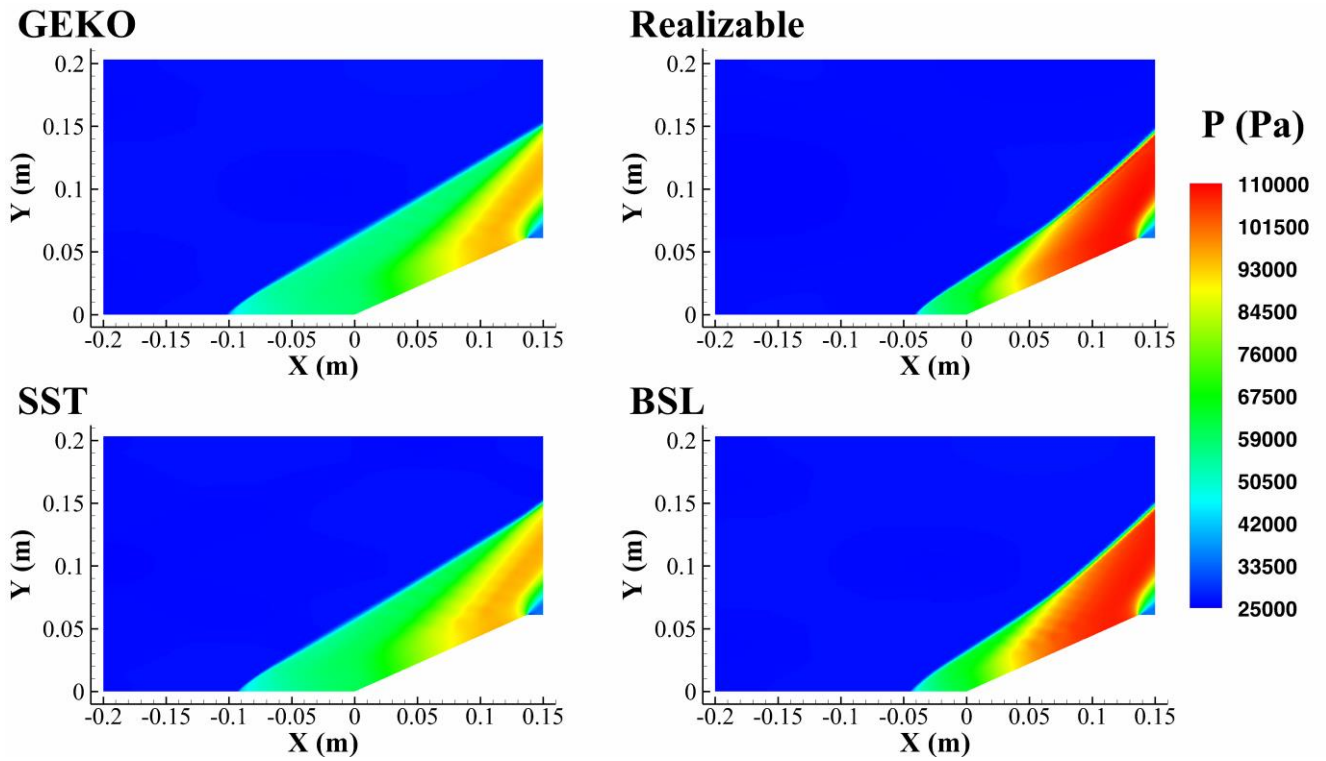
**Fig. 13.** *Skin friction coefficient distribution along the bottom surface*



Fig. 13 shows the skin friction on the bottom surface of the compression ramp domain. As mentioned before, it is apparently seen that GEKO and SST model overpredicted separation length. Also, GEKO and SST model predicted quite low skin friction in the relaxation region and more delayed reattachment point than measured. In contrast with GEKO and SST model, again, BSL and Realizable model show a better agreement, when it comes to the separation shock, separation point, and skin friction distribution after the reattachment point. BSL and Realizable model predicted the point that skin friction is started decreasing, which means the separation shock location is predicted quite well. Looking at it more closely, the BSL model predicted slightly closer the separation shock location than the Realizable model did but the Realizable model predicted the separation point, which is a little bit closer to the experimental data. As for the reattachment point, all models failed to predict the reattachment point perfectly. Having said that, however, the BSL and Realizable model predicted the reattachment point much closer than the GEKO and SST model did, which means that the BSL and Realizable model predicted much shorter separation length.



**Fig. 14.** Mach number contour over 24-deg compression ramp



**Fig. 15.** *Static pressure contour over 24-deg compression ramp*

Mach number contour and static pressure are shown in Fig. 14 and Fig. 15 respectively. In Mach number contour (Fig. 14), all models predict separation shock and reattachment shock, but GEKO and SST model predict a way bigger separation bubble than BSL and Realizable model as seen above Fig. 12 and Fig. 13. Also, the GEKO and SST model under-predict pressure compared to the Realizable and BSL model in the relaxation region. (Fig. 14 and Fig. 15)

# Chapter 5. Uncertainty Quantification for Compressible Flows

## 5.1 gPCE results

The uncertainty quantification is conducted for axisymmetric base flow and the 24-deg compression ramp flow. The several random variables are considered in this present work. The input random variables are  $C_{SEP}$ ,  $C_{NW}$  and  $C_{JET}$ , which are the model coefficients of GEKO model. The probability distribution of each input random variable is assumed as a uniform distribution. A variation range of each input variable follows Table 1. The sample points are taken using LHS. The number of total samples can be set if the order of polynomial chaos and oversampling rate are set.

In this work, for axisymmetric base flow,  $\epsilon_{LOO}$  for axisymmetric base flow is quite higher than 24-deg compression ramp flow.  $\epsilon_{LOO}$  for axisymmetric base flow was higher than 1, but  $\epsilon_{LOO}$  of 24-deg compression ramp flow was lower than 0.1 at the same order and the number of data. Hence, it is investigated that which one is influential factor having an effect on  $\epsilon_{LOO}$  between the order and the oversampling rate for the base flow. Table 10 shows the result. On the left side of the Table 10, it presents the number of samples required corresponding to the order and oversampling rate.

**Table 10.** *the number of sample (left),  $\epsilon_{LOO}$  (right)  
 $P$  : order of polynomial chaos,  $n_p$  : oversampling rate*

# of sample	$p$				
	2nd	3rd	4th	5th	6th
2	20	40	70	112	168
3	30	60	105	168	
$n_p$ 4	40	80	140		
6	60	120			
8	80				

...

$C_{Pbase}$ (RP)	$p$				
	2nd	3rd	4th	5th	6th
2	1.530 (2.071)	2.662 (3.416)	4.282 (6.273)	3.167 (3.861)	3.627 (5.308)
3	0.485 (0.624)	0.896 (1.191)	0.541 (0.722)	0.660 (0.847)	
$n_p$ 4	0.324 (0.456)	0.439 (0.572)	0.313 (0.431)		
6	0.294 (0.410)	0.257 (0.335)			
8	0.267 (0.357)				

On the right side of Table 10, it shows  $\epsilon_{LOO}$  with respect to  $C_{p_{base}}$  and RP.  $\epsilon_{LOO}$  decreases only when the oversampling ratio increases, which means that not increasing the order, increasing the oversampling rate can be a better choice if the number of data is limited or computational cost is expensive.

For Forward problem,  $n_p$  was set to 2 as Schaefer et al. [43] and  $p$  was decided based on QOIs distribution (See Eq 3.12). Fig. 16 shows the distributions regarding to  $C_{p_{base}}$  and RP corresponding to  $p$ . All distributions look quite similar each other. In order to decide specific order for the surrogate model and Bayesian inference, 5<sup>th</sup> order is selected for the base flow. In case of ramp flow, 3<sup>rd</sup> order is chosen due to the limited data.

Total 168 samples for base flow and 60 samples for ramp flow are used to analyze which model closure coefficient is dominant in each flow. Table 11 shows Sobol indices of closure coefficients for QOIs of each compressible flow. The largest contributors to uncertainty in each flow case are typed in bold (Closure coefficients with Sobol indices of less than  $3.0 \times 10^{-3}$  were not considered as being significant [43]). Even though the same numbers of samples are used for OLS and LARS, LARS shows higher  $p$  and lower  $\epsilon_{LOO}$  than OLS. It is apparently seen that  $C_{SEP}$  is the most dominant closure coefficient compared to others. The next dominant closure coefficient is  $C_{NW}$  that affects wall shear stress. Sobol indices of  $C_{NW}$  in case of ramp flow are relatively a little bit higher than the case of base flow. This could be presumed to be affected by the fact that the SWBLI phenomena occurred on the surface of the compression ramp.  $C_{JET}$  has not much contribution to both flow cases as other closure coefficients have.

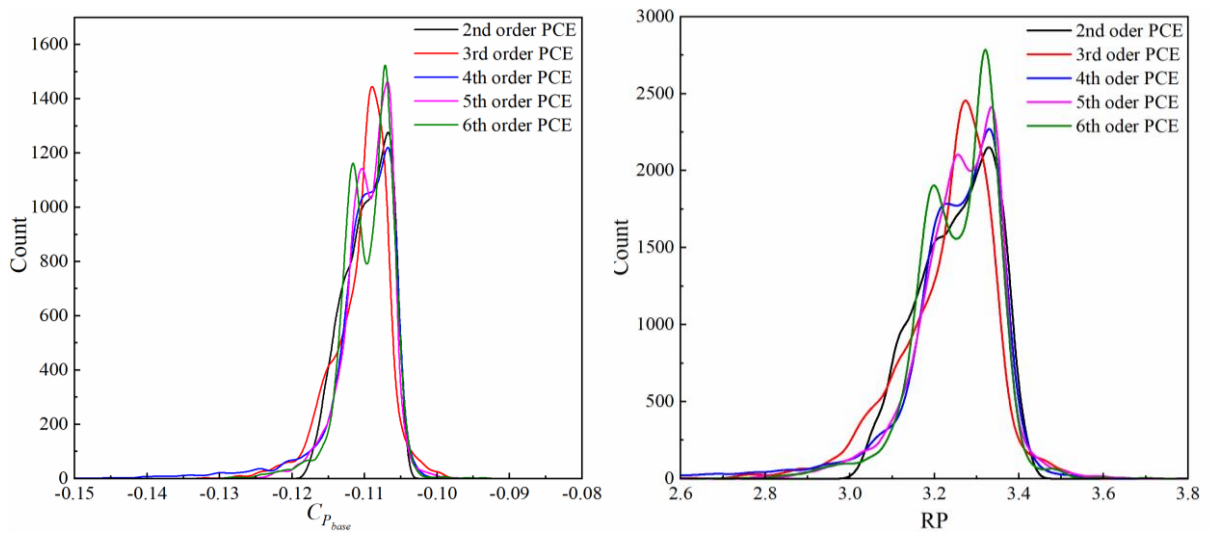


**Fig. 16.**  $C_{P_{base}}$  and RP histogram according to order of polynomial chaos

**Table 11.**  $p$ ,  $\epsilon_{L00}$  and Sobol indices of GEKO closure coefficients for QOIs

	QOIs	$p$	$\epsilon_{L00}$	$C_{SEP}$	$C_{NW}$	$C_{JET}$	
Base	OLS	$C_{P_{base}}$	5	$6.60 \times 10^{-1}$	<b><math>8.63 \times 10^{-1}</math></b>	<b><math>6.34 \times 10^{-2}</math></b>	$5.61 \times 10^{-3}$
		RP	5	$8.47 \times 10^{-1}$	<b><math>8.23 \times 10^{-1}</math></b>	<b><math>7.66 \times 10^{-2}</math></b>	$9.38 \times 10^{-3}$
	LARS	$C_{P_{base}}$	10	$2.59 \times 10^{-2}$	<b><math>9.37 \times 10^{-1}</math></b>	<b><math>4.53 \times 10^{-2}</math></b>	$2.17 \times 10^{-3}$
		RP	14	$3.03 \times 10^{-2}$	<b><math>9.20 \times 10^{-1}</math></b>	<b><math>6.07 \times 10^{-2}</math></b>	$5.35 \times 10^{-3}$
Ramp	OLS	SP	3	$8.22 \times 10^{-3}$	<b><math>9.76 \times 10^{-1}</math></b>	$2.21 \times 10^{-2}$	$5.00 \times 10^{-5}$
		RP	3	$4.43 \times 10^{-2}$	<b><math>8.59 \times 10^{-1}</math></b>	<b><math>1.31 \times 10^{-1}</math></b>	$1.21 \times 10^{-3}$
	LARS	SP	5	$1.67 \times 10^{-4}$	<b><math>9.72 \times 10^{-1}</math></b>	$2.60 \times 10^{-2}$	$5.00 \times 10^{-6}$
		RP	5	$1.54 \times 10^{-3}$	<b><math>8.41 \times 10^{-1}</math></b>	<b><math>1.50 \times 10^{-1}</math></b>	$1.30 \times 10^{-5}$

## 5.2 Bayesian inference

In this thesis, for Bayesian inference, the results obtained by using OLS and LARS are compared. One major advantage of LARS is that users can set the range of orders of polynomial chaos and LARS can give the users a specific order having minimum  $\epsilon_{L00}$ , despite data shortage compared to OLS. Correlated model coefficients through a process of backward problem are shown in Table 12. At the same QOI, the model coefficients between OLS and LARS appeared to be similar values to each other. The posterior distributions of all coefficients does not present similar distributions depending on which algorithm (OLS, LARS) is used but they have a similar distribution tendency to each other according to the same QOI. (Fig. 17 – Fig. 20).

**Table 12.** Correlated model coefficients corresponding QOIs

	QOIs	$C_{SEP}$	$C_{NW}$	$C_{JET}$	
Base	OLS	$C_{P_{base}}$	2.290	-0.684	0.329
		RP	0.723	1.790	0.765
	LARS	$C_{P_{base}}$	2.203	-0.621	0.500
		RP	0.828	0.894	0.408
Ramp	OLS	SP	0.854	0.610	0.456
		RP	0.713	1.508	0.554
	LARS	SP	0.857	0.487	0.499
		RP	0.724	1.252	0.266

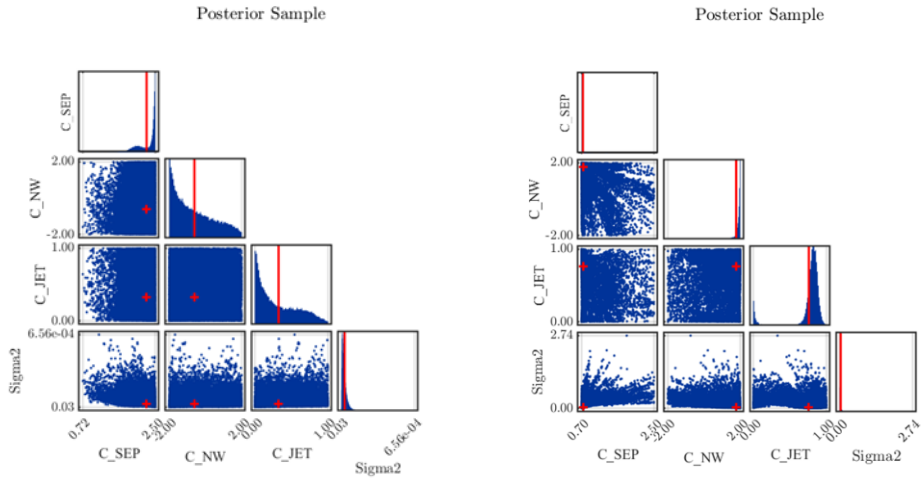


**Fig. 17.** Posterior distribution for  $C_{P_{base}}$  and RP from OLS

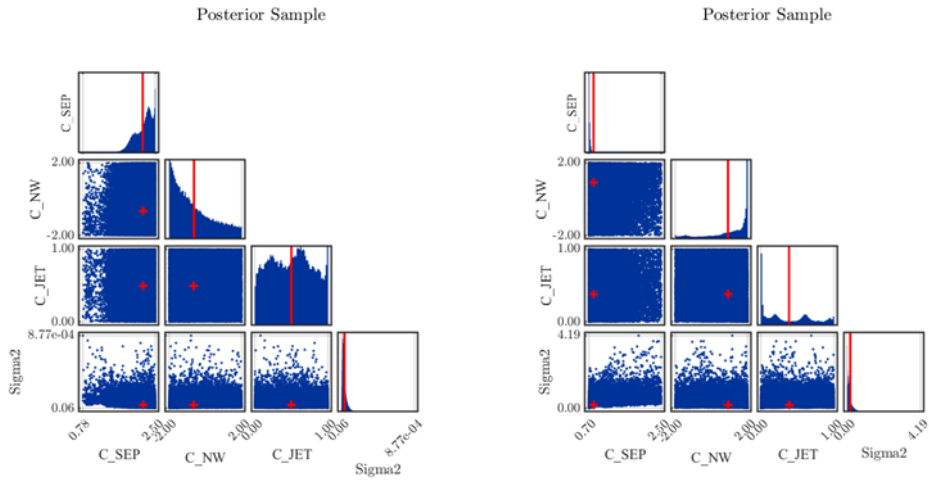


**Fig. 18.** Posterior distribution for  $C_{P_{base}}$  and RP from LARS

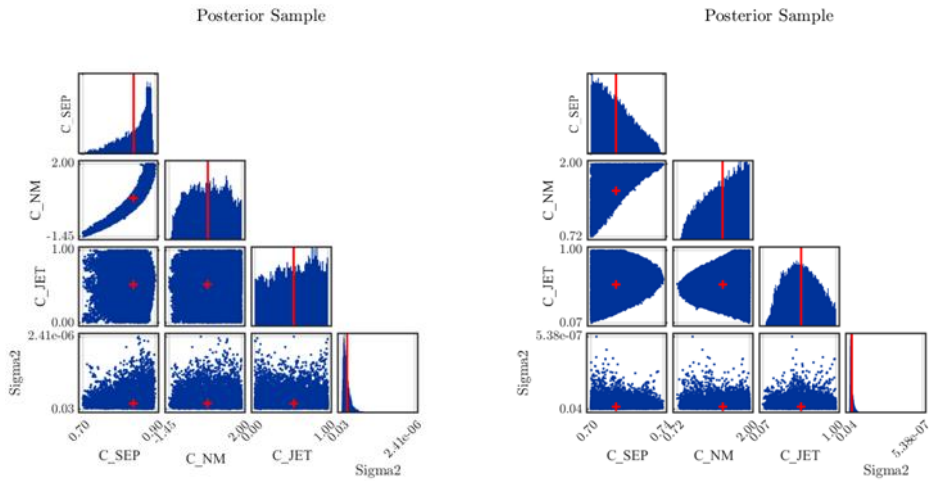


**Fig. 19.** Posterior distribution for SP and RP from OLS

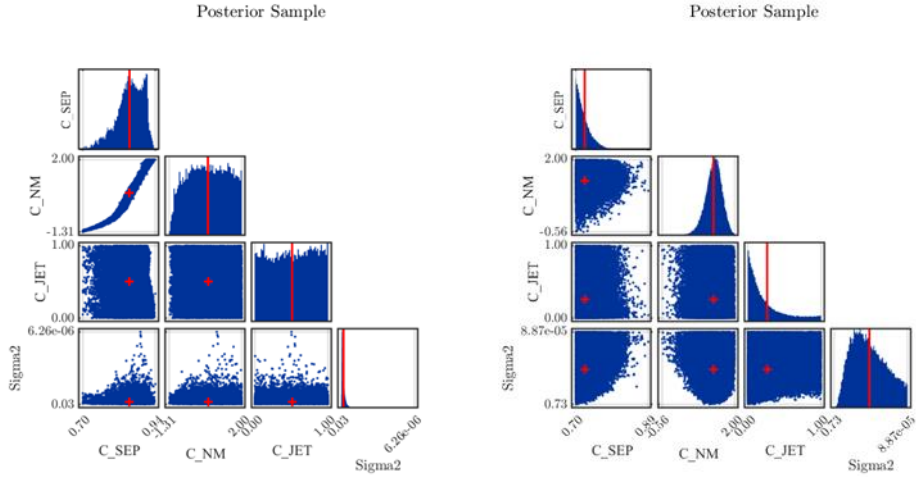


**Fig. 20.** Posterior distribution for SP and RP from LARS

Those coefficients in Table 12 were computed in the deterministic solver (GEKO model) and the results are shown in Fig. 21 and Fig. 22. Fig. 21 shows the pressure distribution along the base surface and the discrepancy is clearly seen between the target QOIs. The pressure distribution of calibrated models for  $C_{P_{base}}$  presents higher pressure than calibrated for RP and also shows more curved distribution. Fig. 21 also shows axial velocity along the centerline. The calibrated models for RP predict closer RP than calibrated models for  $C_{P_{base}}$  and overpredict the peak reverse velocity, which causes lower pressure leading to increased variation in pressure along the base surface.

In Fig. 22, the calibrated models for RP predict so closely to experimental data but underpredict the shock separation position. The calibrated models for SP show a good agreement with SP of experimental data. However they fail to predict RP. Table 13 and 14 present the results of calibrated models. Error (%) which is in the blank shows the discrepancy with respect to each QOI between CFD results and experimental data. Overall, all calibrated models clearly show what they are calibrated for. Also, the calibrated models by OLS and LARS show very similar results, which was indicated because the calibrated model coefficients are not much different. As mentioned in Chap. 3, if computational cost becomes too expensive, LARS drawing reasonable outputs by using less data sets than OLS requires would be a more useful and efficient choice.

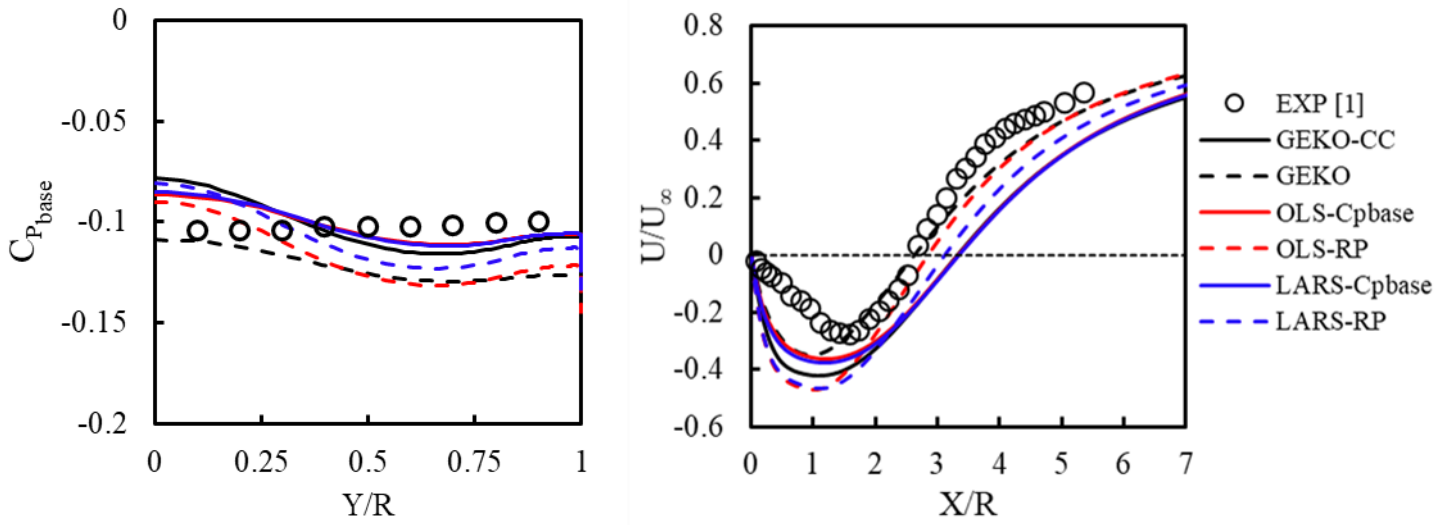


**Fig. 21.** Pressure distribution (left) and centerline velocity (right)

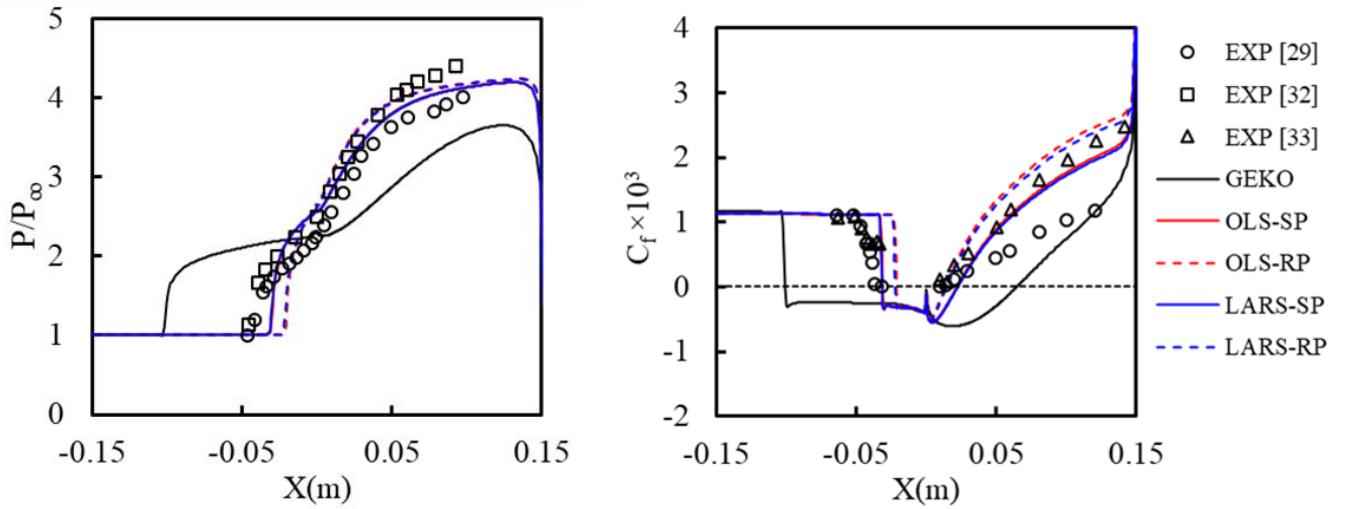


**Fig. 22.** Nondimensional pressure (left) and skin friction coefficient (right) distribution

**Table 13.** Value and error of  $QOIs$  corresponding to each calibrated model (Base flow)

Value (m) (Error %)	Model	Calibrated model				
	GEKO	OLS- $C_{p_{base}}$	OLS-RP	LARS- $C_{p_{base}}$	LARS-RP	
Base	RP	3.322 (25.376)	3.333 (25.787)	2.849 (7.518)	3.341 (26.086)	3.116 (17.589)
	$C_{p_{base}}$	-0.109 (6.550)	-0.106 (3.978)	-0.123 (20.968)	-0.106 (4.124)	-0.115 (12.533)



**Table 14.** Value and error of QOIs corresponding to each calibrated model (Ramp flow)

Value (m)		Model				
(Error %)		Calibrated model				
		GEKO	OLS-SP	OLS-RP	LARS-SP	LARS-RP
Ramp	SP	-0.101 <b>(214.881)</b>	-0.031 <b>(3.081)</b>	-0.021 <b>(33.821)</b>	-0.032 <b>(1.350)</b>	-0.022 <b>(30.724)</b>
	RP	0.065 <b>(587.710)</b>	0.022 <b>(134.371)</b>	0.014 <b>(45.362)</b>	0.023 <b>(140.417)</b>	0.015 <b>(56.179)</b>

## Chapter 6. Conclusion

### 6.1 Conclusions

In the present work, GEKO,  $k-\omega$  BSL,  $k-\omega$  SST and  $k-\varepsilon$  Realizable model were adopted to investigate their ability to predict crucial factors for compressible flows. Those 4 models performed the supersonic flow over the axisymmetric base and the 24deg compression ramp flow. For the axisymmetric base flow, compressibility correction aided the models to predict a even closer level of pressure along the base surface than the models without any correction. However, using compressibility correction caused increasing the radial variation of the pressure due to the increased centerline velocity, which also causes the shear layer reattachment point predicted farther.

As for the compression ramp flow which in the compressibility correction was not applied, GEKO and SST model overpredicted the separation shock point, the separation length and point, and even reattachment point. Also both models underpredicted the pressure and the skin friction in the relaxation region. On the contrary, BSL and Realizable model predicted those well.

Uncertainty Quantification was applied to quantify the coefficients of GEKO model, which are able to be tuned. LHS method was used for sampling input variables assumed a uniform distribution. Regarding each compressible flow studied in this thesis, which model coefficient is dominant, was investigated through the process of the Forward problem. Coefficient  $C_{SEP}$  was the most influential coefficient to the compressible flows. Using surrogate model which was constructed by OLS and LARS, likelihood function and MCMC were calculated. And then each calibrated model coefficient for specific QOIs was able to be known through the posterior distribution of random variables. Calibrated model coefficients through Bayesian inference for each QOI were computed in the deterministic solver, and the results clearly showed what QOIs they were calibrated for. Based on calibrated model coefficients, when  $C_{SEP}$  increases, for axisymmetric base flow, it led to higher pressure levels and overpredicted RP. When it comes to 24deg compression ramp flow, it led to overpredicting the separation length and lower skin friction in the relaxation region.

While the results obtained by GEKO model using calibrated coefficients cannot perfectly match the experimental data, it is apparent that the application of UQ enables more accurate computation of supersonic flows.

## **6.2 Future works**

The further works are needed to identify uncertainty of GEKO model closure coefficients regarding 24-deg compression ramp flow. More data will be added to analyze QOIs distribution corresponding the order of polynomial chaos.

## REFERENCES

- [1] Herrin, J. L., and Dutton, J. C., "Supersonic Base Flow Experiments in the Near Wake of a Cylindrical Afterbody," AIAA Journal., Jan 1994, 32(1), pp. 77-83
- [2] Forsythe, J. R., Hoffmann, K. A., M. Cummings, R., D. Squires, K., "Detached-Eddy Simulation With Compressibility Corrections Applied to a Supersonic Axisymmetric Base Flow," J. Fluids Eng. Dec 2002, 124(4), pp. 911-923
- [3] Simon, F., Deck, S., Guillen, P., and Sagaut, P., "Reynolds-Averaged Navier-Stokes/Large-Eddy Simulations of Supersonic Base Flow," AIAA J., Nov 2006, 44(11), pp. 2578-2590
- [4] Kawai, S., and Fujii, K., "Computational Study of Supersonic Base Flow Using Hybrid Turbulence Methodology," AIAA J, 43(5), June 2005, pp. 1265-1275.
- [5] Tucker, P. K., Shyy, W., "A Numerical Analysis of Supersonic Flow over An Axisymmetric Afterbody," AIAA Paper 93-2347, June 1993
- [6] Papp, J. L., and Ghia, K. N., "Application of the RNG Turbulence Model to the Simulation of Axisymmetric Supersonic Separated Base Flow," AIAA Paper 2001-0727, Jan. 2001
- [7] Simon, F., Deck, S., Guillen, P., and Cayzac, R., "Numerical Simulations of Projectile Base Flow," AIAA Paper 2006-1116, Jan. 2006
- [8] Wilcox, D. C., "Formulation of the  $k-\omega$  Turbulence Model Revisited," AIAA J., Nov 2008, 46(11), 2823-2838
- [9] Wilcox, D. C., Turbulence modeling for CFD, 3<sup>rd</sup> ed., DCW Industries, Inc., La Cañada, CA, 2006.
- [10] Wilcox, D. C., "Dilatation-Dissipation Corrections for Advanced Turbulence Models, AIAA J., Nov 1992, 30(11), pp. 2639-2646.
- [11] Rizzetta, D. P., "Evaluation of algebraic Reynolds-stress models for separated high-speed flows," AIAA 97-2125, 1997

- [12] Rizzetta, D. P., "Evaluation of explicit algebraic Reynolds-stress models for separated supersonic flows," AIAA J., 36(1), 1998, pp. 24-30.
- [13] Marvin, J. G., and Huang, G. P., turbulence modeling-progress and future outlook, proceedings of the fifteenth international conference on numerical methods in fluid mechanics, lecture notes in physics, edited by P. Kutler, J. Flores, and J.-J. Chatot, Springer, New York, 1997, pp. 35-56; also NASA TM 110414, Aug. 1996.
- [14] Gerolymos G. A., Sauret, E., and Vallet, I., "Oblique-shock-wave/boundary layer interaction using near-wall Reynolds stress models," AIAA J. 42, 2004, 1089–1100
- [15] ANSYS® Fluent, Release 19.4, ANSYS, Inc.
- [16] Best Practice: Generalized  $k-\omega$  Two-Equation Turbulence Model in ANSYS CFD (GEKO) 2019
- [17] Menter, F. R., "Two-Equation Eddy-Viscosity Turbulence Models for Engineering Applications", AIAA J., 32(8), Aug 1994, pp. 1598-1605
- [18] Shih, T. H., Liou, W. W., Shabbir, A., Yang, Z., and Zhu, J., "A New - Eddy-Viscosity Model for High Reynolds Number Turbulent Flows - Model Development and Validation". Computers Fluids. 24(3). 227–238. 1995.
- [19] Van Leer, B., "Toward the Ultimate Conservative Difference Scheme. IV. A Second Order Sequel to Godunov's Method". Journal of Computational Physics. 32. 101–136. 1979.
- [20] Chima, R. V., and Liou, M. S., "Comparison of the AUSM+ and H-CUSP Schemes for Turbomachinery Applications". NASA TM-2003-212457. 2003.
- [21] Liou, M. S., and Steffen, Jr. C. J., "A new flux splitting scheme". Journal of Computational Physics. 107(1). 23–39. 1993.
- [22] Liou, M. S., "A sequel to AUSM: AUSM+," Journal of Computational Physics, 129, 1996, pp. 364-382
- [23] ANSYS, 2019, ANSYS Fluent Theory Guide. <http://www.ansys.com/>

- [24] Huan. X., Sargsyan. K., Geraci. G., S. Eldred. M., P. Vane. Z., Lacaze. G., C. Oefelein. J., N. Najm. H., “Global Sensitivity Analysis and Estimation of Model Error, Toward Uncertainty Quantification in Scramjet Computations,” *AIAA J.*, 26, 2018, pp. 1170-1184
- [25] M. Burt. J., and Josyula. E., “Global sensitivity Analysis and Uncertainty Quantification for a Hypersonic Shock Interaction Flow,” *J. Thermophys. Heat Transfer*, 89(3), 2015, pp. 439-449
- [26] UQLab, <https://www.uqlab.com/>
- [27] MATLAB, The MathWorks, Inc., Release 2020b
- [28] McKay, M. D., Schiller, S. B., Welch, W. J., “A comparison of three methods for selecting values of input variables in the analysis of output from a computer code,” *Technometrics*, 31(1), 1979, pp.41-47.
- [29] Hosder, S., Walters, R., Balch, M., “Efficient sampling for non-intrusive polynomial chaos applications with multiple uncertain input variables,” 48th AIAA/ASME/ASCE/AHS/ASC Structures, Structural Dynamics, and Materials conference, Honolulu, Hawaii, USA, AIAA 2007, 2007-1939.
- [30] Settles, G. S., Vas, I. E., and Bogdonoff, S. M., “Details of a Shock-Separated Turbulent Boundary-Layer at a Compression Corner,” *AIAA Journal*, 14(12), 1976, pp. 1709-1715.
- [31] Settles, G. S., Vas, I. E., and Bogdonoff, M., “Shock Wave-Turbulent boundary Layer Interaction at a High Reynolds Number, Including Separation and Flowfield Measurements,” *AIAA Paper 76-164*, Washington, D. C., 1976; also *AIAA Journal*, Vol. 14, Dec. 1976, pp. 1709-1715.
- [32] Horstman, C. C., Settles, G. S., Bas, I. E., T. J., Bogdonoff, S. M., and Hung, C. M., “Reynolds Number Effect on Shock-Wave/Turbulent Boundary -Layer Interactions,” *AIAA Journal*, 15(8), 1977, pp.1152-1158
- [33] Dolling, D. S., and Murphy, M. T., “Unsteadiness of the Separation Shock-Wave Structure in a Supersonic Compression Ramp Flowfield,” *AIAA Journal*, 23(12), 1983,

pp. 1628-1634.

- [34] Settles, G. S., and Dodson, L. J., "Supersonic and Hypersonic Shock/Boundary-Layer Interaction Database," *AIAA Journal*, 32(7), 1994, pp. 1377-1383.
- [35] Pointwise release V18,2
- [36] Roache, P. J., "Verification and Validation in Computational Science and Engineering," Hermosa, Albuquerque, NM, 1998
- [37] Nasa GCI , <https://www.grc.nasa.gov/www/wind/valid/tutorial/spatconv.html>
- [38] Roache, P. J., "Perspective: a method for uniform reporting of grid refinement studies," *Transactions of the ASME Journal of Fluids Engineering*, Vol. 116, 1994, pp.405-413.
- [39] Roache, P. J., "Quantification of uncertainty in computational fluid dynamics," *Annual Review of Fluid Mechanics*, Vol.29, 1997, pp.123-160
- [40] ASME, "Standard for Verification and Validation in Computational Fluid Dynamics and Heat Transfer," ASME V&V 20-2009 (2009)
- [41] Eça, L. and Hoekstra, M., "Discretization uncertainty estimation based on a least squares version of the grid convergence index," *Proceedings of the 2<sup>nd</sup> Workshop on CFD Uncertainty Analysis*, (2006)
- [42] TANAKA, M., and MITAKE, Y., Numerical simulation of thermal striping phenomena in a T-junction piping system for fundamental validation and uncertainty quantification by GCI estimation," *Bull. JSME Mech. Eng. J.*, 2(5), 2015, pp. 1-20.
- [43] Schaefer, J., Hosder and Serhat., and West, T., Rumsey, C., Carlson, J., and Kleb, W., "Uncertainty Quantification of Turbulence Model Closure Coefficients for Transonic Wall-Bounded Flows," *AIAA Journal.*, 55 (1), 2017, pp.195-213